This is a preprint, the final version is subject to change, of the American Mineralogist (MSA)
Cite as Authors (Year) Title. American Mineralogist, in press.
DOI: https://doi.org/10.2138/am-2019-6858

1 **Revision 2**

2 **Reconstruction of the lithosphere-asthenosphere boundary zone beneath**
3 **Ichinomegata maar, Northeast Japan, by geobarometry of spinel peridotite xenoliths**

4

5 Yuto SATO

6 Corresponding author

7 E-mail: syuto@eps.s.u-tokyo.ac.jp

8

9 Kazuhito OZAWA

10 E-mail: ozawa@eps.s.u-tokyo.ac.jp

11

12 (Institutional address)

13 Department of Earth and Planetary Science, Graduate School of Science, the University of

14 Tokyo, 7-3-1 Hongo, Bunkyo-ku, Tokyo 113-0033, Japan.

15 Tel: +81-3-5841-4501

16

This is a preprint, the final version is subject to change, of the American Mineralogist (MSA)
Cite as Authors (Year) Title. American Mineralogist, in press.
DOI: https://doi.org/10.2138/am-2019-6858

Abstract

Estimation of accurate derivation depths of spinel peridotite xenoliths, for which reliable geobarometers are not available, is imperative to reconstruct precise structures of the lithosphere-asthenosphere boundary (LAB) zones, such as thermal, chemical, rheological, and petrological structures, for better understanding dynamics operating there. We challenged this problem for spinel peridotite xenoliths from Ichinomegata maar in the back-arc side of Northeast Japan Arc. Extensive mineral chemical examinations of nine xenolith samples revealed various patterns of chemical zoning in pyroxenes suggesting diverse thermal histories. We examined the timescales of development of each zoning pattern to identify minerals, mineral portions, and chemical species attaining equilibrium as close as possible just before the xenolith extraction. Applying the best pair of geothermobarometers to the chosen analyses (Ca-Mg-Fe components from the outermost rims of orthopyroxene and clinopyroxene), plausible derivation depths of eight samples were obtained. They range 0.72-1.6 GPa in pressure and 830-1080 °C in temperature, which define a high thermal gradient of 10 K/km or 290 K/GPa. There is an intimate correlation between the zoning patterns of pyroxenes and the depth estimates: pyroxenes in the deeper samples have zoning indicating cooling followed by heating just before the

xenolith extraction and those of the shallower samples have zoning indicating simple cooling.

Depth variations of rock microstructures, grain size of olivine, chemical compositions of minerals, and phase assemblage including the presence or absence of glass or fluid phase show that the mantle beneath Ichinomegata consists of two distinct layers. The shallower (28-32 km) layer is granular, less oxidized, amphibole- and plagioclase-bearing, and subsolidus, whereas the deeper (41-55 km) layer is porphyroclastic, amphibole- and plagioclase-free, oxidized, and partially molten. The contrasts between the two layers suggest that the upper layer represents a lithospheric mantle and the lower layer a LAB zone. They are similar to those reported from the bottom of the subcontinental lithospheric mantle in various aspects, but the boundary layer beneath Ichinomegata is much shallower (40-60 km) and cooler (~1100 °C). The coincidence of the depth of rheological transition marked by the change from granular to porphyroclastic textures and that of the melting phase transition of hydrous peridotite system, marked by the complementary presence or absence of H_2O-rich fluid/amphibole and that of melt in localized pockets, is the remarkable feature of the boundary zone beneath Ichinomegata. This suggests that a rheological boundary zone in arc settings is governed by melting of the hydrous mantle and

51 that the underlying asthenosphere is partially molten. The depth-dependent thermal history
52 shown by chemical zoning in pyroxenes and the presence of melt as pockets suggest that
53 the LAB beneath Ichinomegata was in transient state and under development through
54 dynamic processes of heat and material transportation.

55

56 **Keywords:**

57 spinel peridotite xenolith
58 geobarometry
59 upper mantle structures
60 lithosphere-asthenosphere boundary

61

This is a preprint, the final version is subject to change, of the American Mineralogist (MSA)
Cite as Authors (Year) Title. American Mineralogist, in press.
DOI: https://doi.org/10.2138/am-2019-6858

Introduction

Lithosphere-asthenosphere boundary (LAB) is usually defined by seismological observations, across which shear wave velocity and attenuation change rapidly, and is attributed to changes in either temperature, water contents, extent of partial melting, chemical compositions, or grain size (Green et al., 2010; Hirschmann, 2010; Hirth and Kohlstedt, 1996; Karato, 2010, 2012; O'Reilly and Griffin, 2006). In the framework of plate tectonics, LAB represents a boundary zone having certain thickness, where heat, momentum, and materials are exchanged between conductive mantle (lithosphere) and underlying convective mantle (asthenosphere) (Anderson, 1995; Fischer et al., 2010; McKenzie and Bickle, 1988; O'Reilly and Griffin, 1996). The boundary zone is thus regarded as a thermal boundary layer or a rheological boundary layer (McKenzie and Bickle, 1988; Sleep, 2005, 2006). Processes taking place in the boundary zone play important roles in heat and material transportation from the Earth's interior, but are not well understood.

Mantle xenoliths are fragments of mantle materials brought to the Earth's surface by alkali basalt or kimberlite from either lithosphere or, potentially, asthenosphere (O'Reilly and Griffin, 2010). They may be useful sources of information about the LAB zone.

Because appropriate barometers are available for garnet-bearing lithologies mostly brought up by kimberlite magmas, structures of the LAB zone beneath cratons (e.g., Kaapvaal, Siberia, and Slave) have been well examined. The thermal and rheological structure near the LAB of the subcontinental lithospheric mantle (SCLM) were firstly revealed by Boyd (1973), who found an inflection in geotherm with low-pressure limb composed of granular samples on a conductive and high-pressure limb of sheared samples on steeper, transient geotherms. He proposed that the inflection marks the top of the low-velocity zone located at the bottom of SCLM. Later geochemical studies revealed the depth variations of xenoliths in kimberlites; high-pressure xenoliths are fertile and low-pressure ones are depleted (e.g., Griffin et al., 1999, 2003; O'Reilly and Griffin 2010). These depth variations of material properties have been providing critical information on the origin of the cratonic LAB (e.g., O'Reilly and Griffin, 2010).

The situation drastically changes for a thin and younger lithosphere, where alkali basalts sampled mostly spinel peridotite xenoliths (Phanerozoic lithosphere; e.g., arc, intraplate basin and plateau, and continental margin; Nixon, 1987; O'Reilly and Griffin, 2006). Garnet-absent peridotites are stable at depths shallower than ~60 km, and reliable geobarometers are not available for them (e.g., O'Reilly et al., 1997). Because of this,

96 structures of shallow LAB zones are poorly constrained. One way to avert this difficulty is
97 to combine geotherm calculated using heat flow data and temperature estimates from
98 xenoliths on the assumption that the current geotherm is at steady state since the period of
99 the xenolith extraction (e.g., Behr and Hirth, 2014; Titus et al., 2007). However, this
100 assumption is inappropriate if dynamic processes were operated to cause a temporal change
101 of the thermal structure of lithosphere. This study aims at the quantitative reconstruction of
102 the mantle structure beneath the Ichinomegata maar in Northeast Japan on the basis of
103 estimation of the derivation pressure of each spinel peridotite xenolith by applying
104 geothermobarometers to mineral chemical data with special care for specification of the
105 best chemical analyses representing equilibrium just before the xenolith extraction.
106 Ichinomegata maar in Northeast Japan is one of the well-studied spinel peridotite
107 xenolith localities in arc settings. Since the 1980s, many studies on mantle xenoliths from
108 Ichinomegata have documented thermal, petrological, geochemical, and rheological
109 diversities in the mantle beneath Ichinomegata. Takahashi (1980) extensively examined the
110 thermal aspect on the basis of mineral chemical data. He showed a large variation of
111 temperatures ranging 740-1000 °C estimated by various thermometers, such as a
112 two-pyroxene thermometer (Wells, 1977) and a thermometer based on Fe-Mg partitioning

between olivine and spinel (Fabriès, 1979). Later compilation of estimated temperatures for peridotite xenoliths from Megata maars including Ichinomegata by Arai et al. (2007) gave the similar temperature range of 700-1020 °C estimated using the two-pyroxene thermometer of Wells (1977). Takahashi (1980) identified two xenolith groups showing distinct thermal histories: one recorded simple cooling and the other cooling followed by heating.

Takahashi (1986) also carefully examined the petrologic aspects of Ichinomegata xenoliths. He demonstrated that two pyroxene-spinel symplectite, which occurs in some peridotite samples and had been thought as a breakdown product of garnet (e.g., Kuno, 1967; Kuno and Aoki, 1970), is a breakdown product of plagioclase. He also examined the occurrences of glass and amphibole in Ichinomegata xenoliths and contended partial melting of the amphibole-bearing mantle. Abe et al. (1992) described various modes of occurrence of amphibole and argued that the involvement of water-bearing silicate melts and water-rich fluids released from them played a role in the formation of hydrous phases.

Diverse geochemical features are revealed by several studies. Tanaka and Aoki (1981) reported that spinel peridotite xenoliths lacking pyroxene-spinel symplectite have light rare earth element (LREE) -enriched rare earth element (REE) patterns, but that

130 symplectite-bearing peridotites have LREE-depleted patterns. Abe et al. (1998) later
131 confirmed this systematic relationship and also reported LREE-enrichment patterns in
132 harzburgite containing abundant amphibole ± phlogopite. Satsukawa et al. (2017) reported
133 LREE-depleted REE patterns of clinopyroxene with a weak negative anomaly of Eu, a
134 strong negative anomaly of Sr, and highly variable positive anomalies of Th and U from
135 plagioclase peridotites. They discussed partial melting, open-system reaction, and modal
136 and cryptic metasomatisms in the wedge mantle.

137 Radiogenic isotope ages of peridotite xenoliths from Ichinomegata have been examined
138 for Rb-Sr, Sm-Nd, and Re-Os systems. Abe and Yamamoto (1999) reported Rb-Sr mineral
139 isochron ages of 300-200 Ma for several xenolith samples. Brandon et al., (1996) obtained
140 ca. 400 Ma from a linear array of Sm-Nd isotopic ratios of clinopyroxene separated from
141 several Ichinomegata xenoliths, but they attributed the array to a mixing process because
142 the $^{187}Os/^{188}Os$ and Re/Os ratios give negative model depletion ages.

143 The wide variations of microstructures related to deformation including lattice preferred
144 orientations (LPO) of olivine were reported from Ichinomegata xenoliths (Satsukawa and
145 Michibayashi, 2014). Satsukawa and Michibayashi (2014) found that the olivine LPOs are
146 dominantly A-type with subordinate D-type, and attributed them to shallow mantle

147 deformation during the Japan Sea opening.

148 The diversity in various aspects of the mantle beneath Ichinomegata must be understood
149 in the firm framework of the space (and time) to be useful information for better
150 understanding dynamics operated in the vicinity of the LAB. However, geobarometry of
151 Ichinomegata mantle xenoliths is very scarce and limited to minimum pressure estimation
152 by using density and H_2O mole fraction of fluid inclusions (Kumagai et al., 2014), which
153 gives 0.66-0.78 GPa (23-28 km in depth). It is, therefore, imperative to establish proper
154 geobarometry for Ichinomegata xenoliths, based on which thermal, petrological,
155 geochemical and rheological structures may be reconstructed.

156 Chemical heterogeneity of constituent minerals of examined peridotite xenoliths is
157 presented first in this paper. Then, minerals, their grain parts, and chemical components
158 best recording chemical equilibrium just before xenolith extraction are specified by
159 evaluating the timescales of formation of the chemical heterogeneity in minerals. This is
160 followed by geothermobarometry with error estimation and verification of the depth
161 estimates by comparing with petrologic and stratigraphic information of the xenoliths.
162 Finally, thermal, chemical, rheological, and petrological structures of the LAB zone of the
163 shallow lithospheric mantle are reconstructed, and their implications are discussed.

164

165 **Geology and samples**

166 Ichinomegata maar is one of the maars formed in the latest Pleistocene (80-60 ka;
167 Kitamura et al., 1990) on the Oga Peninsula in the back-arc side of the Northeast Japan arc
168 (Fig. 1). The depth of Mohorovičić discontinuity (MOHO) was estimated to be 25-30 km
169 by seismological observations (Iwasaki et al., 2013; Zhao et al., 1992). The depth of
170 seismic lithosphere-asthenosphere boundary (LAB) beneath Ichinomegata is constrained to
171 be shallower than 60 km (1.8 GPa), which is the depth of LAB beneath the Japan Sea
172 marked by a jump in shear wave velocity (Yoshizawa et al., 2010; Zheng et al., 2011); a
173 shallowing tendency of the velocity jump towards the volcanic arc is suggested by the
174 anisotropic shear-wave tomography.

175 Fragments of peridotites, pyroxenites, granulites, and hornblende-rich mafic and
176 ultramafic rocks are found as xenoliths in calc-alkaline andesite-dacitic pyroclastic rocks
177 distributed around Ichinomegata maar (Hayashi, 1955; Kuno, 1967; Kuno and Aoki, 1970;
178 Aoki, 1971; Katsui et al., 1979). Spinel peridotite is the most common peridotite xenoliths,
179 but a few plagioclase-bearing peridotites occur. Hydrous phases such as amphibole and
180 phlogopite are often observed as minor constituents (Aoki and Shiba, 1973; Abe et al.,

1992). We examined nine peridotite xenoliths (eight lherzolites and one wehrlite; Table 1) from Ichinomegata. Hydrous phases are minor in the examined samples, indicating that they did not experience extensive hydration as observed in harzburgite xenoliths veined by hydrous phases (Abe et al., 1992). All of the samples used in this study belong to the collection of the University of Tokyo. The late professor Hisashi Kuno collected some of them, and their petrography is described by Kuno and Aoki (1970) and Takahashi (1986).

Analytical methods

All samples were prepared as thin sections of ~40 μm thickness and polished with diamond pasts of 1 μm size. The thin sections were observed for characterization of their microstructures using an optical microscope and scanning electron microscope with a field-emission electron gun (FE-SEM; JEOL JSM-7000F) at the University of Tokyo.

Concentrations of 11 elements (Si, Ti, Al, Cr, Fe, Mg, Ca, Mn, Ni, Na, and K) were quantified using an electron probe microanalyzer (EPMA; JEOL JXA-8900L) at the University of Tokyo. Accelerating voltage of 15-20 kV and beam current of 12-50 nA were adopted. Peak and background counting times were 10-20 and 5-10 seconds, respectively, with x2-x4 accumulations, while they were 40 and 20 seconds with x2-x4 accumulations

198 for minor elements (e.g., CaO in orthopyroxene and olivine). Chemical compositions were
199 calculated with the oxide ZAF (atomic number, absorption, and fluorescence) correction
200 method using oxides (TiO_2, Al_2O_3, $(Fe^{2+},Mg)(Cr,Al,Fe^{3+})_2O_4$, Fe_2O_3, and MgO) and
201 silicates (wollastonite, albite, and adularia) as standards. The Fe^{3+} content was calculated
202 based on stoichiometry for spinel but ignored for the other minerals because they contain
203 too small amounts of Fe^{3+} to be estimated accurately from EPMA analyses by assuming
204 stoichiometry. Pyroxene analyses were made avoiding lamellae visible under the
205 microscopes. The adopted intervals in line analyses of pyroxenes range from 7-22 μm.
206 Modal compositions (Table 1) were estimated from areas of minerals occupying in each
207 thin section. Each mineral was identified by combining X-ray maps for five elements (Mg,
208 Al, Ca, Cr, and Fe) obtained in mapping analyses of EPMA over the entire thin sections
209 (Supplementary Fig. S1). Size distributions and mean grain sizes of olivine were measured
210 by processing digitized images of olivine grain boundaries traced on Mg X-ray maps under
211 the optical microscope with crossed polarizers.
212
213 **Petrography**
214 **Modal compositions**

This is a preprint, the final version is subject to change, of the American Mineralogist (MSA)
Cite as Authors (Year) Title. American Mineralogist, in press.
DOI: https://doi.org/10.2138/am-2019-6858

The examined samples are composed dominantly of olivine (50-81 vol.%), orthopyroxene (2-40 %), clinopyroxene (6-16 %), and spinel (1-4 %) (Figs. 2a, 2b, and S1). They are classified as lherzolite except for one wehrlite sample (HK64081205b, denoted as HK64 in Takahashi, 1986). Minor amounts of plagioclase and amphibole are present in some samples (Table 1). Three of the nine samples (HK64081206g, HK64081206c, and HK66031502) contain plagioclase, which always occurs either in contact with or enclosed in pyroxene-spinel symplectite (see Fig. 3f in Takahashi, 1986). Such symplectite (Figs. 2c and 2d) is shown to be a reaction product of plagioclase and olivine (Takahashi, 1986). These samples are thus grouped as plagioclase lherzolite in this paper. The other samples have neither plagioclase nor symplectite and are grouped as spinel lherzolite (HK64081206d, IC81-5, HK64081205a, IC81-8, and HK66031501) or spinel wehrlite (HK64081205b) (Table 1).

Two types of plagioclase occurrences are recognized (Fig. 2e). “Primary” plagioclase, which only occurs in HK64081206g, is anhedral and never coexists with olivine (Fig. 2e). “Secondary” plagioclase coexists with olivine and fills grain boundaries between pyroxenes and spinel of partly decomposed symplectite associated with a small amount of glass (Fig. 2e; see Figs. 2a and 2b of Abe et al., 1992). It also overgrows on the “primary”

232 plagioclase. The "primary" plagioclase is rich in anorthite (An) component and brighter
233 than the An-poor "secondary" plagioclase in back-scattered electron images (BEIs, Fig.
234 2e).

235 All of the plagioclase lherzolites contain amphibole (Table 1). Two of them
236 (HK64081206c and HK66031502) have pargasitic amphibole rimming two-pyroxene
237 spinel symplectite (Fig. 2d; cf. Abe et al., 1992; Kumagai et al., 2014). The occurrence of
238 amphibole in spinel lherzolite is limited to HK64081206d, which is always in contact with
239 spinel. Amphibole also occurs as lamellae in the core region of clinopyroxene in
240 plagioclase lherzolites (Table 1) and as rounded inclusions (~50 μm in diameter) in
241 clinopyroxene in a spinel lherzolite sample HK64081205a. These modes of occurrence of
242 amphibole (lamellae and inclusions in clinopyroxene) indicate isolation from equilibrium
243 with the other major constituent phases, and they are excluded in the later discussions
244 related to the stability of amphibole.

245

246 **Microstructures**

247 Two types of the overall microstructure are recognized from the examined samples.
248 They are granular and porphyroclastic textures with one sample showing a transitional type,

249 which is called weakly porphyroclastic texture in this paper (Table 1; Figs. 2a and 2b). The
250 sample mean grain size of olivine varies depending on the textures (Table 1).

251 The mean grain sizes of olivine of four granular samples (HK64081206g, HK64081206c,
252 HK66031502, and HK64081205b; Fig. 2a) range 0.38-0.53 mm showing relatively narrow
253 size distributions (1σ = 0.35-0.37 mm). Four porphyroclastic samples (IC81-5,
254 HK64081205a, IC81-8, and HK66031501; Fig. 2b) are characterized by the presence of
255 pyroxenes porphyroclasts and have a smaller mean grain size of olivine ranging 0.21-0.30
256 mm and wider size distribution (1σ = 0.15-0.25 mm) than those of the granular samples.
257 The weakly porphyroclastic sample (HK64081206d; Fig. S1) is characterized by mean
258 olivine size of 0.31 mm, which is smaller than that of granular samples and comparable to
259 that of porphyroclastic samples and relatively narrow grain size distribution (1σ = 0.24
260 mm) comparable to that of granular samples.

261

262 **Glass and voids/fluid inclusions**

263 Glass in mantle xenoliths suggests partial melting of the mantle, and microstructures
264 such as voids, fluid inclusions, and etch pits along grain boundaries suggest saturation in a
265 fluid. They could be stable phases in the mantle if they were not formed or introduced

during final xenolith extraction processes. Their presence or absence in each sample was carefully examined, and relevant microstructures are described below and summarized in Table 1.

Four of the examined spinel lherzolites (HK64081205a, IC81-8, HK66031501, and HK64081205b) have glass (Fig. 2f). The glass is not homogeneously distributed and confined in pyroxene-rich layers defining a banding (Fig. S1). This glass forms pockets with 50-500 μm in size always contacting with pyroxene grains. Mineral grains contacting the glass pockets commonly show facetted crystal morphology (Fig. 2f, see also Takahashi, 1986). The glass contains vesicles and euhedral clinopyroxene, spinel, and amphibole with the size of <10 μm and morphologies suggesting rapid growth. Plagioclase is not observed in the glass. Sample HK64081206d contains glass- and void-bearing crystal-dominant aggregate (Takahashi, 1986). The constituent crystals of the aggregate are clinopyroxene, amphibole, olivine, and spinel. They are 10-50 μm in size and are euhedral and equant in spite of the high crystallinity, which is contrasting to the quench crystals in the glass pockets. These microstructures indicate slower growth under low supersaturation in crystallization to form the crystal-dominant aggregate as suggested by Takahashi (1986).

This is a preprint, the final version is subject to change, of the American Mineralogist (MSA)
Cite as Authors (Year) Title. American Mineralogist, in press.
DOI: https://doi.org/10.2138/am-2019-6858

The two plagioclase lherzolite samples HK64081206c and HK66031502 and two spinel lherzolite samples HK64081206d and IC81-5 have voids or open-gaps along grain boundaries with aligned depressions on the open surfaces (Table 1; Fig. 2g). The depressions on olivine are 1-10 μm across and have a diamond-like outline. They align along straight and narrow grooves (width 0.1-0.4 μm). These features are very similar to the evaporation pits and related surface morphology developed at dislocation outcrops on (001) of forsterite and olivine with $Mg/(Mg+Fe^{2+})$ ~0.9 (Ozawa and Nagahara, 2000; Ozawa et al., 2012), suggesting that they are etch pits developed at surface outcrops of dislocations owing to dissolution in contact with a fluid phase. Fluid inclusions are also common in olivine grains with etch pits (Fig. 2h). They occur as negative crystals resembling the surface etch pits in size, shape, and distribution. These microstructures suggest the presence of fluid.

Mineral chemical compositions

Spatial elemental distributions in pyroxenes and olivine grains were carefully examined with X-ray maps and line profiles. We found significant heterogeneities, which are mostly concentric and are called “zoning” hereafter. The extent and pattern of zoning strongly

depend on grain size. Coarser pyroxene grains (>1 mm) show wider compositional variation and more complex patterns. Such zoning patterns have information on thermal history that each xenolith underwent, the clarification of which is indispensable to specify appropriate minerals, mineral parts, and components for application of geothermobarometry to estimate pressure and temperature just before the xenolith extraction. We thus describe zoning in pyroxenes in detail before mean chemical compositions of other constituent minerals and their correlations are presented.

Chemical zonings in orthopyroxene

Four chemical zoning types in orthopyroxene denoted as type O1-O4 are identified on the basis of the distinct zoning patterns of Ca and summarized in Table 2. Each xenolith contains orthopyroxene showing one of the four zoning types. Type O1 is characterized by a continuous decrease of Ca, Al, Cr, Fe, and Ti from the core to the rim (Fig. 3a). Type O2 is characterized by a gradual decrease of Ca, Al, Cr, Fe, and Ti from the core to the margin followed by a weak increase to the outermost rim (Fig. 3b). Type O3 is characterized by a continuous decrease of Ca, Al, Cr, and Ti from the core to the margin followed by a strong increase to the outermost rim (Fig. 3c). Type O4 is characterized by a slight increase of Ca

316 and a slight decrease of Al and Cr from the core to the rim (Fig. 3d). The variations of Si
317 and Mg are complementary to those of Ca, Al, Cr, and Fe irrespective of zoning types.
318 Significant fluctuations in the Ca profile and scatter in the Al and Cr profiles in Figure 3 are
319 due to the presence of dense and thin lamellae of clinopyroxene and spinel, which cannot
320 be completely avoided in the host orthopyroxene analyses.
321
322 **Chemical zonings in clinopyroxene**
323 Three types of zoning in clinopyroxene denoted as type C1-C3 are identified on the
324 basis of the distinct zoning patterns of Ca and are summarized in Table 2. Each xenolith
325 contains clinopyroxene showing one of the three zoning types. Type C1 coexists with type
326 O1 or O2, and types C2 and C3 do so with types O3 and O4, respectively (Table 2). Type
327 C1 is characterized by a gradual and intense increase of Ca, Mg, and Si and decrease of Al,
328 Cr, Fe, Na, and Ti from the core to the rim (Fig. 4a). Type C2 is characterized by a slight
329 decrease or a flat pattern of Ca from the core to margin with an intense decrease of Ca
330 toward the outermost rim. Al and Cr show a slight decrease, slight increase, or a flat pattern
331 from the core to margin and intense increase towards the outermost rim with or without
332 minima near the rim (Fig. 4b). The variation pattern of Ti is similar to that of Cr, and the

pattern of Na is similar but more diffusive than Al. The patterns of Mg and Si are complementary to the pattern of Al. Type C3 is characterized by flat patterns of Ca, Mg, Si, Ti, and Na throughout grains and a slight decrease of Al and Cr contents from the core to the margin where Cr is flat and Al shows a slight increase toward the outermost rim (Fig. 4c). Spiky fluctuations in the Ca, Al, and Cr profiles for the Type C1 and C2 clinopyroxenes (Figs. 4a and 4b) are due to the presence of lamellae minerals. In the core of Type C1 and C2 clinopyroxenes (Figs. 4a and 4b), negative and positive spikes of Ca, Al, and Cr in the zoning profiles indicate chemical heterogeneity present around the lamellae minerals.

Mean chemical compositions

The mean chemical compositions of cores of olivine (8-10 analyses), cores, mantle, and rims of pyroxenes (3-5 analyses, respectively), and the other constituent minerals (1-20 analyses) for each sample are listed in Table 3. Some of them are plotted in Figure 5 with standard deviations $\pm 1\sigma$. The core, mantle, and rim compositions of pyroxenes were obtained by taking means of respective segments having minimum or maximum concentrations of key elements (Ca, Al, or Cr depending on zoning types) in line profiles

350 (Figs. 3 and 4). Each segment is >50 μm wide for the core, ~10 μm wide for the mantle,
351 and 10-100 μm wide for the rim.

352 Olivine is homogeneous in Mg# = Mg/(Mg+Fe^{2+}) and CaO and Al_2O_3 contents except
353 for in the margin (approximately several tens μm). The Mg# of olivine core ranges
354 0.87-0.91, which is within the reported range 0.83-0.91 for Ichinomegata peridotite
355 xenoliths (e.g., Kuno and Aoki, 1970; Aoki and Shiba, 1974; Abe et al., 1992). The sample
356 mean CaO contents of olivine core vary from 0.03 to 0.10 wt.%, and their distributions are
357 split into two ranges: one is 0.03-0.04 and the other is 0.08-0.10 wt.% (Figs. 5a and 5d).
358 The Al_2O_3 contents of olivine core range 0.002-0.016 wt.% showing a positive correlation
359 with the CaO contents (Fig. 5a). The CaO contents of olivine core are the same as those
360 reported by Takahashi (1980, 1986) including the split distribution.

361 Chemical compositions of orthopyroxene vary 0.41-1.1 in CaO wt.%, 0.98-5.1 wt.% in
362 Al_2O_3 wt.%, and 0.14-0.57 wt.% in Cr_2O_3 wt.%. The CaO contents at the rim of
363 orthopyroxene vary from 0.41 to 1.1 wt.% and are split into two value ranges; 0.41-0.61
364 and 0.93-1.1 wt.% (Figs. 5b, 5d, and 5e). The higher range exactly corresponds to those
365 found in samples identified as “preheated” xenoliths by Takahashi (1980, 1986). The Al_2O_3
366 and Cr_2O_3 contents at the rim of orthopyroxene vary 1.2-5.1 and 0.23-0.49 wt.%,

367 respectively. Chemical compositions of clinopyroxene vary 20.5-23.8 in CaO wt.%, 1.4-6.8
368 in Al_2O_3 wt.%, and 0.26-2.4 in Cr_2O_3 wt.%. The CaO, Al_2O_3, and Cr_2O_3 contents at the rim
369 of clinopyroxene vary 20.9-23.6, 1.2-5.9, and 0.26-0.80 wt.%, respectively.

370 The sample mean compositions of the cores of large spinel (> 200 μm) are listed in
371 Table 3. The Cr# = Cr/(Cr+Al) mostly range 0.18-0.23 with one exception of
372 HK64081206d, which has a high Cr# of 0.59. The Cr# of spinel and Mg# of olivine are
373 plotted mostly within the narrow band of the olivine-spinel mantle array (Arai, 1994; Fig.
374 6). Exceptions are HK64081206d and HK64081205b, whose olivine compositions are too
375 low in Mg# to be plotted in the mantle array. Abe et al. (1992) reported the same pattern of
376 co-variation of olivine and spinel compositions.

377 Plagioclase in the plagioclase lherzolites is very heterogeneous in anorthite content (An
378 = Ca/(Ca+Na)). The primary plagioclase defined above has zoning in An content (Fig. 2e),
379 which increases from the core (An = 0.76) to the margin (An = 0.87). The secondary
380 plagioclase is homogeneous and has a consistent An ranging 0.62-0.65 irrespective of its
381 occurrence. Amphibole in the plagioclase lherzolites contains ~3 wt.% Na_2O (Table 3) and
382 is classified as pargasite according to Leake et al. (1997). The amphibole compositions are

383 within the range reported in the previous literature (e.g., Aoki and Shiba 1973; Takahashi,
384 1986; Abe et al. 1992).

385 Chemical compositions of glass (Table 3) were obtained by taking means of the multiple
386 analyses of the central area of glass in pockets avoiding visible chemical heterogeneity
387 owing to the host minerals, quench crystals, and vesicles. The glass present in the pockets
388 in HK64081205a, IC81-8, and HK66031501 has Fe-rich basaltic-andesitic composition
389 with Mg# ranging 0.53-0.56, whereas that in HK64081205b has a Fe-rich alkali basalt
390 composition with Mg# of 0.45. The former contains 5 wt.% of quartz, whereas the latter
391 contains 10 wt.% of nepheline in CIPW normative compositions. The glass compositions
392 for sample HK64081205b show slightly higher Al_2O_3 contents than that reported by
393 Takahashi (1986) (HK64 in Table 1 of Takahashi, 1986). The weight deficiency of all glass
394 compositions by EPMA analyses (~2-5 wt.%; Table 3) is comparable to that by Takahshi
395 (1986).

396

397 **Chemical correlations**

398 Chemical correlations between the CaO content of olivine core and CaO, Al_2O_3, and
399 Cr_2O_3 contents of rims and cores of pyroxenes are shown in Figure 5. The CaO and Al_2O_3

400 contents at the core of olivine show a clear positive correlation (Fig. 5a). The CaO, Al_2O_3,
401 and Cr_2O_3 contents at the rim of orthopyroxene show notable positive correlations with
402 each other, but those at the core show very weak correlations (Fig. 5b). The CaO contents
403 at the rim of clinopyroxene show negative correlations with Al_2O_3 and Cr_2O_3, but such
404 correlations are not clear for those at the core (Fig. 5c). The CaO content at the rim of
405 orthopyroxene shows a good positive correlation with the CaO contents of the core of
406 olivine (Fig. 5d). The CaO contents at the rim of two pyroxenes show a strong negative
407 correlation (Fig. 5e). The Al_2O_3 and Cr_2O_3 contents of pyroxenes at the rim show clear
408 positive correlations (Fig. 5f), but they are weaker than that of CaO at the rim of pyroxenes
409 (cf. Fig. 5e).
410

411 **Geothermobarometry**

412 Before geothermobarometry of the xenoliths, the following procedures were taken to
413 specify minerals, their grain portions, and chemical components best recording chemical
414 equilibrium just before the xenolith extraction: (1) decoding thermal history of the
415 xenoliths from chemical zonings in minerals with estimation of timescales for the zoning
416 development, (2) selection of minerals, components, and grain portion representing

417 equilibrium just before the final heating for xenolith extraction, (3) specification of
418 appropriate geothermobarometers. The errors were estimated by using Monte Carlo method.
419 The depth estimates were verified by comparing with petrologic information from the
420 xenoliths.
421
422 **Decoding thermal history records in pyroxenes**
423 Chemical zonings are principally formed by deviation of old equilibrium compositions
424 to a new equilibrium at the rim induced by changes in temperature, pressure, and/or bulk
425 chemical composition through homogenization by diffusion between the rim at local
426 equilibrium and inside the mineral grains unless extensive grain boundary migration does
427 not take place. This is an appropriate model of zoning development in mantle peridotites
428 owing to their high melting temperature since they are principally in a solid state, which is
429 substantiated for Ichinomegata xenoliths by the reported Rb-Sr mineral isochron ages
430 (200-300 Ma; Abe and Yamamoto, 1999).
431 The final event that the xenoliths underwent is heating and decompression by
432 incorporation into a host magma and transportation to the surface. This event has a very
433 short timescale (Spera, 1984). Ozawa (1984) examined the kinetics of Mg-Fe exchange

reaction between olivine and spinel in lherzolite xenoliths from Ichinomegata and estimated that the duration of magma transportation was 1 day for HK66031501 and 1-4 hours for HK66031502 at 1200 °C and that the duration was 1 day for HK66031502 at 1100 °C. Given this timescale and temperature for xenolith extraction processes, zonings in pyroxenes over scales greater than 5 μm (the upper limit of spatial resolution of EPMA) as observed in the grain margin if any (Figs. 3 and 4; Table 2) cannot be attributed to the exhumation process, because diffusivity of these elements in pyroxenes are more than 1-2 orders of magnitude smaller than that of Mg-Fe interdiffusion in olivine and spinel (Chakraborty, 2010; Van Orman and Crispin, 2010; Cherniak and Dimanov, 2010).

Since the peridotite xenoliths were in plagioclase-spinel stability fields, the steady increase in Ca, Al, and Cr towards the outermost rim in orthopyroxene of types O2 and O3 all implies temperature increase continued until just before the xenolith extraction (e.g., Gasparik, 2003; Lindsley, 1983; Klemme and O'Neill, 2000). This is consistent with the steady decrease in Ca and the increase in Al and Cr in clinopyroxene of type C2 (Table 2; e.g., Gasparik, 2003; Sachtleben and Seck, 1981). The zoning types O2, O3, and C2 are all characterized by increases of Ca, Al, and Cr towards the outermost rim over the distance of 20-200 μm. Therefore, xenolith samples containing pyroxenes with zoning types O2 or O3

and C2 underwent temperature increase shortly before their extraction, which took place much longer duration than the final exhumation event. For similar reasons, xenolith samples containing type O4 zoning characterized by a slight but a steady increase in Ca over the distance of ~500 μm towards the outermost rim in orthopyroxene underwent a more prolonged temperature increase than xenoliths containing types O2 or O3 and C2 pyroxenes. The nearly constant Ca of type C3 may be explained by the high CaO abundance of clinopyroxene masking the small variation in the margin of type O4 orthopyroxene coexisting with type C3.

Zoning in orthopyroxene grains of type O1 characterized by a steady decrease of Ca, Al, and Cr in their margin (Fig. 3; Table 2) implies a steady temperature decrease without any detectable temperature increases. The Ca, Al, and Cr zonings in clinopyroxene of type C1 also suggest the same thermal history. The samples having pyroxenes with types O1 and C1 zoning, therefore, underwent continuous cooling, which is principally consistent with Takahashi (1980). The zonings were either almost instantaneously frozen by the xenolith extraction or frozen in a past cooling event when passing through a closure temperature specific for each component. The cooling process, therefore, could have been on the way until shortly before the xenolith extraction or taken place a long time ago down to much

lower temperatures than the closure temperatures. These two possibilities must be resolved for proper geothermobarometry of these samples, which is addressed below.

Minerals and components for geothermobarometer

As discussed in the last section, heating events shortly before the xenolith transportation are suggested for samples including type O3 orthopyroxene and type C2 clinopyroxene and those including type O4 orthopyroxene and C3 clinopyroxenes. On the other hand, a continuous cooling event before the xenolith transportation is suggested for samples including type O1 orthopyroxene and type C1 clinopyroxene. Xenolith samples containing type O2 orthopyroxene and type C1 clinopyroxene suggest an intermediate thermal history of these two extreme cases: weak heating following continuous cooling at mantle depths. We need to take the difference in patterns of thermal history into consideration when appropriate mineral chemical compositions are chosen for geothermobarometers.

The chemical compositions representing pressure and temperature where the xenoliths resided in the mantle are most plausibly recorded at the rim of pyroxenes, if heating or cooling were in progress till the xenoliths were extracted (Smith, 1999) and if transportation of relevant components along mineral interfaces are fast enough to follow

485 local equilibrium. Since diffusion of Al and Cr are slower than that of interdiffusion of
486 Mg-Fe and Ca-(Mg, Fe) by more than 1 to 2 orders of magnitude (Brady and McCallister,
487 1983; Dimanov and Sautter, 2000; Ganguly et al., 2007; Sautter et al., 1988; Smith and
488 Barron, 1991), reactions relevant to Ca, Mg, and Fe could be fast enough to maintain local
489 equilibrium and form rim zoning measurable with EPMA. Therefore, Ca-Mg-Fe
490 components at the rim of pyroxenes are more suitable for geothermobarometry than Al-Cr
491 components. This is confirmed below by examining correlations of these components at
492 pyroxene rims.

493 The rim compositions of pyroxenes in the examined samples show correlations in Ca, Al,
494 and Cr (Figs. 5b to 5f) irrespective of zoning types (Table 2), but correlations among core
495 concentrations are not necessarily good (Figs. 5b to 5f). The remarkable correlations of Ca
496 concentrations between the pyroxene rims for all the zoning types (Fig. 5e) strongly
497 support that the Ca-(Mg, Fe) components were exchanged between orthopyroxene and
498 clinopyroxene fast enough to follow local equilibrium at the rims. The weaker correlations
499 of Ca-Mg-Fe components with Al and Cr (Figs. 5b and c) suggest more deviation from the
500 equilibrium for Al and Cr components, supporting our choice of the components for
501 geothermobarometry. Moreover, the excellent correlations of the Ca-(Mg, Fe) components

including zoning types of O1 or O2 orthopyroxene and C1 clinopyroxene strongly suggest that the profiles of these zoning types were on the way of formation by a cooling event continued until before the xenolith extraction. They may not represent zoning frozen during a past cooling event proceeded down below the closure temperatures. This inference is also supported by the good correlation between Ca contents at the rim of orthopyroxene and those at the homogeneous core of olivine (Fig. 5d). The reactions involving Ca-Mg-Fe components in pyroxenes, therefore, provide the best geothermobarometers for the peridotite xenoliths from Ichinomegata irrespective of zoning types.

The choice of Ca-Mg-Fe components at the rim of pyroxenes for geothermobarometry has several merits. First, it is applicable to any pressure irrespective of the presence or absence of particular aluminous phases: garnet, spinel, or plagioclase. Second, the Ca-Mg-Fe components are not much affected by whole-rock chemical composition, whereas Al and Cr components are difficult to be calibrated for geothermobarometry because of their strong dependence on fertility of peridotites. Third, diffusivities of Ca, Mg, and Fe in clinopyroxene and orthopyroxenes are within the same order of magnitude in a wide range of temperatures (Cherniak and Dimanov, 2010), and thus the Ca-Mg-Fe components in pyroxenes comparably respond to temperature and pressure changes.

This is a preprint, the final version is subject to change, of the American Mineralogist (MSA)
Cite as Authors (Year) Title. American Mineralogist, in press.
DOI: https://doi.org/10.2138/am-2019-6858

519

520 **Selection of geothermobarometers**

521 As discussed in the last subsection, the basic strategy required for estimation of
522 derivation pressures and temperatures is to utilize the pressure- and temperature-sensitive
523 reactions involving Ca-Mg-Fe components in both pyroxenes (e.g., Mercier et al., 1984).
524 Possible candidates based on such reactions are two-pyroxene geothermobarometers
525 (Bertrand and Mercier, 1985; Brey and Köhler, 1990; Nickel and Brey 1984) and
526 Ca-in-orthopyroxene geothermobarometers (Brey and Köhler, 1990; Lindsley, 1983). A
527 pair of geothermobarometers must be selected from these candidates. We selected
528 two-pyroxene geothermobarometer (T_{BKN}) and Ca-in-orthopyroxene geothermobarometer
529 ($T_{Ca\text{-}in\text{-}Opx}$) both calibrated by Brey and Köhler (1990) as the most appropriate pair. They
530 are empirical geothermobarometers calibrated for the expected pressure and temperature
531 ranges beneath Ichinomegata (<1.8 GPa; 740-980 °C according to Takahashi, 1986) and
532 based on the same experiments, which may reduce systematic errors in paring the two
533 geothermobarometers.

534

535 **Results of pressure and temperature estimation**

Pressures and temperatures obtained by applying the two geothermobarometers to pairs of pyroxenes rims are listed for successful eight samples in Table 4 with errors and plotted in Figure 7. The estimated pressures range from 0.72 to 1.6 GPa and temperatures from 828 to 1081 °C. One unsuccessful exception (HK64081206d) out of the examined nine xenoliths gives a negative pressure and 811 °C (Table 4). This is probably attributed to that the clinopyroxene rims analyzed so far lacks any zoning reflecting temperature increase suggested by the zonings of Al and Cr in orthopyroxene with much slower diffusivity than Ca (Table 2). This is partly attributed to grain boundary migration notably extensive for this sample (Sato and Ozawa, 2018). In the following examination of depth variations of various features of the xenoliths, we exclude this sample.

The pressure and temperature are split into two groups (Fig. 7). Three samples (HK64081206g, HK64081206c, and HK66031502) give lower temperatures ranging 828-905 °C, and the other samples (IC81-5, HK64081205a, IC81-8, HK66031501, and HK64081205b) give distinctively higher temperatures ranging 1017-1081 °C. The two groups correspond to the two sample groups in CaO contents of olivine and orthopyroxene (Fig. 5d). All successful pressure estimates are well above the pressure at the seismic MOHO depth (25 km and 0.6 GPa) beneath Ichinomegata and lower than that at the

553 seismic LAB depth beneath the Japan Sea (60 km and 1.8 GPa). Although the distinction of
554 the two temperature groups and their estimated temperature ranges are consistent with
555 those of the previous studies (Takahashi, 1980, 1986), our study quantitatively constrains
556 the derivation depths of the xenoliths, which allows estimation of the thermal structure
557 beneath Ichinomegata.
558
559 **Error estimation**
560 The uncertainty of pressure and temperature estimates for each xenolith sample
561 (standard deviation, ±1 σ; 68% confidence interval; Table 4) is evaluated with a
562 Monte-Carlo method assuming that the source of errors is from analytical uncertainties
563 with Gaussian distributions. The standard deviations (Figs. 7a and 7b) and error ellipses
564 (Fig. 7b) are based on 3-5 chemical compositions at the outermost rim of different
565 pyroxenes grains (Tables 3 and 4; Supplementary Table S1). Thus, the chemical
566 heterogeneity in the outermost rim of pyroxenes is the main source of uncertainties for
567 pressure and temperature estimates. The standard deviations range 0.2-0.7 GPa for
568 pressures and 12-30 °C for temperatures. There is an inevitable tendency that low
569 temperature and pressure samples have greater uncertainties because the CaO contents at

570 the outermost rim of orthopyroxene grains are low and somewhat variable. Although most
571 of the samples have large standard deviations overlapping with each other particularly in
572 pressure, the overall thermal gradient is meaningful because it is highly oblique to the
573 major axes of error ellipses (Fig. 7b). This suggests that the variations of derivation
574 pressure and temperature for the xenolith samples are not originated from random chemical
575 variations of pyroxenes, but from mineral chemical variations systematically correlated
576 with each other reflecting the actual pressure and temperature conditions (Fig. 5).
577
578 **Depth structure of the mantle beneath Ichinomegata maar**
579 The estimated derivation pressures allow us to determine the depth variation of material
580 properties of the xenoliths, such as thermal, geochemical, petrological, and rheological
581 features just before the xenolith extraction. The depth estimates actually have systematic
582 relationships with temperature, mineral chemistry, mineral assemblage, rock texture, and
583 grain size (Figs. 8 and 9, Table 5), suggesting stratification of the mantle beneath
584 Ichinomegata. They are described in this section.
585
586 **Thermal structure**

587 Figures 7 and 8 show the estimated thermal structure of the mantle beneath
588 Ichinomegata (Tables 4 and 5). The examined samples were derived from two depth
589 segments; a shallow low-temperature segment (828-905 °C, 0.72-0.85 GPa, 28-32 km) and
590 a deep high-temperature segment (1017-1081 °C, 1.16-1.62 GPa, 41-55 km). Four of the
591 five latter samples experienced a heating event before the xenolith extraction ("preheating";
592 Takahashi, 1980). If all the pressure and temperature estimates are linearly regressed, the
593 thermal gradient is given by 9.6 ±1.2 K/km or 290 ±37 K/GPa. The thermal structure gives
594 the temperature of 810 ±24 °C at the seismically estimated MOHO (25 km or 0.6 GPa) and
595 1158 ±26 °C at the upper limit of the seismically estimated LAB (60 km or 1.8 GPa) (Fig.
596 7a). The overall high thermal gradient within thin seismological lithospheric mantle (< 35
597 km thick) is much higher than the steady geotherm within SCLM near LAB (3-5 K/km;
598 Boyd, 1973; Kopylova et al., 1999; O'Reilly and Griffin, 2006). Although the shallow
599 low-temperature segment does not provide any meaningful geotherm, the deep
600 high-temperature segment gives a thermal gradient of 3.8 ±0.9 K/km or 115 ±26 K/GPa. It
601 is far gentler than the overall geotherm, probably suggesting non-linearity of the thermal
602 structure.
603

This is a preprint, the final version is subject to change, of the American Mineralogist (MSA)
Cite as Authors (Year) Title. American Mineralogist, in press.
DOI: https://doi.org/10.2138/am-2019-6858

604 **Mineral chemical structure**

605 The Mg# of olivine show no or little systematic change with depth if the deepest sample
606 with the lowest Mg# is excluded (Fig. 8; Table 5). This sample HK64081205b shows
607 peculiar mineral chemical compositions in addition to the lowest Mg# of olivine. The
608 olivine is low in NiO and high in MnO contents (Table 5). This sample is also plotted
609 outside of and to the Fe-rich side of the olivine-spinel mantle array (Fig. 6). These
610 characteristics suggest that this sample is of cumulus origin. There remains a weak
611 decreasing tendency of the Ni content and an increasing tendency of the MnO content of
612 olivine if the deepest sample is excluded. These weak depth variations are attributable to
613 the observed temperature variation of ~300 K through temperature-dependent partitioning
614 with coexisting olivine, pyroxenes, and spinel (Ballhaus et al., 1991; Kawasaki et al., 1994;
615 von Seckendorff and O'Neill, 1993). We thus infer that the chemical stratification of the
616 mantle beneath Ichinomegata in terms of olivine composition is insignificant. The depth
617 variation of Cr# of spinel is also insignificant (Fig. 8), which is partly due to its
618 susceptibility to subsolidus reactions related to the formation and decomposition of
619 plagioclase as well as temperature.

620 Application of oxybarometer after Ballhaus et al. (1991) to chemical compositions of

spinel and olivine of the deep-level samples gives oxygen fugacity ranging from +0.31 to +0.69 in log unit from FMQ buffer ($\delta\log(fO_2)_{FMQ}$). This range is as high as that of Parkinson and Arculus (1999). By contrast, the $\delta\log(fO_2)_{FMQ}$ for the shallow-level samples (28-41 km) ranges from -1.3 to +0.19, which is systematically lower than that of the deep-level samples and comparable to that of abyssal peridotite (Parkinson and Arculus, 1990). The oxygen fugacity thus tends to increase with depth (Fig. 8).

Melting phase transition and composition of fluid phase

The presence of glass and open gaps with etch-pitted walls and fluid inclusions in some samples could indicate the presence of melt and fluid phase, respectively, before the xenolith extraction. The fluid phase occurs in the shallow levels (30-41 km), whereas the melt phase occurs in the deep levels (45-55 km) (Table 5, Fig. 8). Note that shallowest sample HK64081206g does not have microstructures indicating the presence of fluid and amphibole excepting lamellae. The mutually complementary depth distributions of melt and fluid are very remarkable, suggesting melting phase transition. They, however, might have formed during the xenolith exhumation processes such as heating, decompression, and melt/fluid introduction from the host magma. Takahashi (1986) argued that the glass had

638 formed at mantle depths because of the chemical compositions of glass and the textures
639 suggesting long residence at high temperature. The possibilities of partial melting and
640 fluid/melt introduction during the xenolith extraction are negated on the basis of the
641 following three lines of evidence.

642 First, the compositions of glass are different from those of the host magma and the
643 essential ejecta of Ichinomegata maar (Takahashi, 1986; Sakuyama and Koyaguchi, 1984).
644 Secondly, temperatures estimated from the glass composition (Table 3) to be saturated with
645 olivine by using a thermometer (equation (15) of Putirka, 2008) range 1047-1115 °C with
646 water contents estimated from the weight deficiency in EPMA analyses of the glass (2-5
647 wt.%) and our pressure estimation. They are consistent with the temperatures at the
648 derivation depths estimated for the glass-bearing xenoliths. These temperatures are
649 significantly lower than the temperatures estimated for the primitive basaltic end member
650 of xenolith host magma (Sakuyama and Koyaguchi, 1984; 1140 and 1220 °C according to
651 equation (13) of Putirka, 2008). Finally, all of the glass-bearing samples show
652 homogeneous and high CaO contents of olivine at the core, suggesting that such high
653 temperatures were maintained for a significant time (>1000 years; Takahashi, 1980).
654 Therefore, we conclude that the melt phase was present before the xenolith extraction and

655 is attributed neither to instantaneous melting nor melt injection during the extraction by the
656 host magma.

657 The glass-bearing samples do not contain amphibole but those with fluid inclusions and
658 etch pits (HK64081206c and HK66031502) do so excepting the shallowest sample
659 HK64081206g, which contains amphibole as lamellae in clinopyroxene but has neither
660 fluid inclusions nor etch pits. The amphibole occurrence as quench crystals in the
661 glass-bearing samples suggests that the melt contains a significant amount of H_2O. Such
662 consistent mutually complementary relationships of the glass and amphibole accompanying
663 fluid inclusions/etch pits strongly suggests that the fluid phase was present before the
664 xenolith extraction and that it was H_2O-rich. H_2O-rich fluid inclusions have been reported
665 from peridotite xenoliths from Ichinomegata, such as pyroxene hosted saline fluid
666 inclusions (Kumagai et al., 2014). Moreover, the depth range for the samples with evidence
667 for the presence of fluid phase (30-41 km) is greater than the minimum depth estimates
668 (23-28 km at ~920 °C) from the fluid inclusions of the amphibole-bearing xenoliths
669 (Kumagai et al., 2014). It is concluded that there is a melting phase transition of H_2O-rich
670 fluid-saturated peridotite system (wet solidus) beneath Ichinomegata.

671

672 **Subsolidus phase transition**

673 Aluminous phases show a systematic variation with depth (Fig. 8 and Table 5).
674 Plagioclase and its breakdown products (pyroxene-spinel symplectite) appear exclusively
675 in the shallow levels (28-32 km), whereas spinel appears as an aluminous phase in the deep
676 levels (41-55 km). The shallowest sample with the lowest temperature estimate (28 km;
677 HK64081206g) contains primary plagioclase partially decomposed into symplectite, but
678 the other plagioclase lherzolite samples do not contain primary plagioclase, which was
679 totally decomposed into symplectite. This may indicate that the pressure is resolved even in
680 the shallow segments (Fig. 7). The chemical structure as demonstrated above does not
681 support bulk-composition control on the presence or absence of plagioclase (see discussion
682 below), which was observed in the Horoman peridotite complex (Ozawa and Takahashi,
683 1995). We conclude that there is a pressure sensitive phase transition from spinel to
684 plagioclase facies at ~40 km depth (at least somewhere within 32-41 km) beneath
685 Ichinomegata.

686

687 **Rheological structure**

688 Rock textures of the examined samples show a systematic depth variation (Fig. 8 and

689 Table 5); granular texture occurs mostly in the shallow levels (28-32 km; Fig. 2a) and
690 porphyroclastic texture dominates in the deep levels (41-52 km; Fig. 2b) except for the
691 deepest granular sample (55 km; HK64081205b), which is of cumulus origin as mentioned
692 above. This is also substantiated by the variation of olivine grain size, which shows a
693 systematic decrease with depth. The shallow granular samples (28-32 km) have larger grain
694 sizes (0.38-0.47 mm in diameter), and the deep porphyroclastic samples (41-52 km) have
695 smaller sizes (0.21-0.30 mm). These rock textures of the shallower granular samples are
696 consistent with those studied by Satsukawa and Michibayashi (2014), most of which
697 contain plagioclase or its breakdown products excepting one spinel lherzolite sample
698 showing the most deformed microstructure.
699

700 **Validation of estimated pressures and temperatures**

701 In spite of our careful treatment of the chemical compositions and the
702 geothermobarometry, considerable pressure errors are estimated particularly for shallow,
703 low-temperature samples. In this section, we first use phase transitions tightly constrained
704 by experiments to confirm our pressure estimation. They are (1) melting phase transition
705 from subsolidus fluid-saturated and amphibole-bearing peridotite to above-solidus fluid-

and amphibole-absent peridotite and (2) phase transition from plagioclase to spinel peridotite. After the test of consistency with the phase relations and the estimated pressures and temperatures, we further show that the estimated derivation depths are consistent with the stratigraphic control of the occurrence of two groups of xenoliths with or without records of the heating event in the Ichinomegata maar deposits (Koyaguchi, 1986).

Validation using melting phase transition

In the examined peridotite xenoliths, the transition of fluid-present to melt-present states occurs at the pressure of 1.2 GPa and temperature of 1035 °C (Fig. 9a, Table 5). This bounding condition is significantly lower than that of dry peridotite solidus (~1270 °C at 1.2 GPa according to Hirschmann, 2000), suggesting partial melting of the hydrous mantle. Amphibole and microstructures indicating the presence of H_2O-rich fluid coexist in the samples without glass (Table 1) except for one sample giving the lowest pressure and temperature (HK64081206g), which suggests that at least the deeper part of plagioclase peridotites was saturated with H_2O. By contrast, the absence of amphibole and no evidence for fluid presence in glass-bearing samples indicate that the deeper part was not saturated with H_2O. Therefore, the melting phase transition identified in our samples must be located

723 somewhere between H_2O-saturated (Green, 1973; Grove et al., 2006) and –undersaturated
724 solidus (Niida and Green, 1999; Green et al. 2010; Wallace and Green, 1991); this implies
725 that the amphibole and fluid-bearing samples must be plotted below the former solidus and
726 that the glass-bearing samples above the latter solidus.

727 In Figure 9a, the glass-free, amphibole- and fluid-bearing samples are consistently
728 plotted below the experimentally determined water-saturated solidi (Green, 1973; Grove et
729 al., 2006). This validates the estimated pressures and temperatures of the amphibole- and
730 fluid-bearing samples, which are under the water-saturated subsolidus condition.

731 Niida and Green (1999) demonstrated that the water-undersaturated solidi, which are
732 controlled by decomposition of amphibole (Mysen and Boecher, 1975), depend on the bulk
733 alkaline contents (Na_2O + K_2O wt.%) enhancing the stability of amphibole. Actually, the
734 maximum amphibole stability temperature at ~2.0 GPa corresponding to the solidus
735 condition varies from 1025 °C for bulk Na_2O + K_2O = 0.33 wt.% to 1150 °C for 1.17 wt.%
736 (Niida and Green, 1991). The bulk Na_2O + K_2O contents of Ichinomegata xenoliths range
737 0.09-0.24 wt.% (Kuno and Aoki, 1970), which is comparable to that of Wallace and Green
738 (1991) (0.33 wt.%) and significantly lower than that of Niida and Green (1999) (0.66 wt.%).
739 Therefore, the low-temperature solidus under the water-undersaturated condition of

740 Wallace and Green (1991) is adopted for the melting phase transition in Ichinomegata
741 xenoliths. All of the glass-bearing samples are consistently plotted above the
742 water-undersaturated solidus after Wallace and Green (1991). This validates the estimated
743 pressures and temperatures of the glass-bearing samples, which are plotted above the
744 solidus condition and water-undersaturated in Fig. 9a.
745
746 **Validation using subsolidus phase transition**
747 Borghini et al. (2010) experimentally determined the stability field of plagioclase of a
748 fertile dry peridotite system (Ti, Cr-NCFMAS system; FLZ of Borghini et al. 2010), which
749 is lower than 0.7-0.8 GPa at 900-1200 °C (Fig. 9b). Contrary to this, Niida and Green
750 (1999) determined the stability field of plagioclase in hydrous peridotite system, which is
751 lower than 0.9-1.0 GPa at 900-1100 °C (Fig. 9b). The estimated pressures of the three
752 samples of plagioclase lherzolite from Ichinomegata (0.74-0.85 GPa) are within the
753 stability field of plagioclase according to Niida and Green (1999) (Fig. 9b) but are within
754 the spinel stability field according to Borghini et al. (2010).
755 The phase boundary between plagioclase and spinel facies is strongly affected by the
756 system composition, particularly Na_2O and CaO contents; an increase in bulk Na_2O/CaO

757 shifts the stability limit of plagioclase toward a high-pressure side (Fumagalli et al., 2017).
758 The Na_2O/CaO ratio in starting materials of Niida and Green (1999) (0.117) is higher than
759 that of Borghini et al. (2010) (0.076-0.093). The examined samples from Ichinomegata
760 have low Na_2O/CaO ratios (0.061-0.078; Kuno and Aoki, 1970) comparable to that of
761 Borghini et al. (2010). Because the examined peridotites contain a certain amount of H_2O,
762 its effect on the plagioclase-spinel phase boundary must be evaluated. The amount of Na
763 and Ca available for plagioclase crystallization was affected by H_2O only through the
764 formation of Na and Ca-bearing hydrous phases. The Na/Ca ratio of pargasitic amphibole is,
765 however, comparable to that of starting materials in the experiments of Niida and Green
766 (1999), and thus the presence of H_2O does not affect the phase boundary in their
767 experiments. The phase transition between plagioclase and spinel lherzolites from
768 Ichinomegata, therefore, must be evaluated according to Borghini et al. (2010), which is
769 0.7-0.9 GPa at 900-1200 °C (Fig. 9b). Our pressure estimates for two of the plagioclase
770 lherzolite samples are, however, plotted far above this range apparently being inconsistent
771 with the experimental results. The presence of pyroxene-spinel symplectite in the
772 plagioclase lherzolites indicates that they were originally equilibrated in the plagioclase
773 stability field and later brought into the spinel stability field. This puts a constraint that the

774 pressure and temperature conditions just before the xenolith exhumation must be in the
775 higher-pressure side of the spinel-plagioclase facies boundary according to Borghini et al.
776 (2010).

777 Temperature decrease, pressure increase, or both is required for reaction between olivine
778 and plagioclase to form pyroxene-spinel symplectite (Gasparik, 2003). It should not have
779 taken place during xenolith extraction, which causes temperature increase and pressure
780 decrease. The zoning profiles of pyroxenes in the plagioclase lherzolites feature continuous
781 decreases in Ca, Al, and Cr towards the rim for orthopyroxene and increase in Ca and
782 decrease in Al and Cr for clinopyroxene (Zoning types of O1, O2, and C1; Table 2 and Figs.
783 3 and 4). These zoning patterns are reproduced by cooling with a limited decrease in
784 pressure not to increase Al towards the rim.

785 The upper limit of temperature (and pressure) condition before the cooling is
786 constrained by solidus of plagioclase peridotite since there is no evidence for melting
787 before the formation of symplectite in plagioclase lherzolite samples. The solidus of the
788 plagioclase lherzolites is somewhere between wet and dry solidi (Fig. 9; Green, 1973;
789 Jaques and Green, 1980). The upper limit of pressure (and temperature) conditions for the
790 plagioclase lherzolites can be placed by dP/dT of the Al isopleth for orthopyroxene as

791 shown by the upper dotted line in Fig. 9b starting from the intersection of dry solidus
792 (Jaques and Green, 1980; a thick dashed curve in Fig. 9b) and plagioclase-spinel facies
793 boundary (Borghini et al., 2010) at ~1200 °C and ~0.85 GPa. The shaded area in this
794 diagram defines the widest possible pressure and temperature conditions just before the
795 xenolith extraction for the plagioclase lherzolites.

796 This pressure and temperature regions for symplectite-bearing lherzolites includes the
797 estimated pressures and temperatures for the plagioclase lherzolites and is much lower than
798 those of the spinel lherzolites and wehrlite (Fig. 9b). Even if a wet solidus according to
799 Green (1973) (thin curve in Fig. 9b) is used as the upper limit instead of the dry solidus,
800 estimated pressures and temperatures of all of the plagioclase lherzolites are within the
801 narrower possible regions (meshed pattern; Fig. 9b). This validates the pressure and
802 temperature estimation not only for the plagioclase lherzolites but also for the spinel
803 lherzolites and the wehrlite.

804 The plagioclase lherzolite sample giving the lowest pressure and temperature estimates
805 (0.72 GPa, 829 °C; HK64081206g) almost lies on the boundary of plagioclase and spinel
806 stability field after Borghini et al. (2010). The sample contains the highest abundance of
807 primary plagioclase (~0.5 vol. %) with limited reaction extent. The suppressed extent of

808 plagioclase decomposition in HK64081206g is consistent with its lowest estimates of
809 pressure and temperature among the plagioclase lherzolites.
810
811 **Validation using stratigraphic control of the occurrence of two xenolith types**
812 Koyaguchi (1986) documented the occurrence of xenoliths with different thermal
813 histories controlled by the stratigraphy of Ichinomegata pyroclastic rocks. Peridotite
814 xenoliths which experienced a heating event tend to occur in the upper stratigraphic
815 horizon, and those without such heating in the lower horizon. On the basis of this
816 observation, Koyaguchi (1986) argued that a group of xenoliths with glass recorded a
817 prolonged heating event in a stratified magma chamber and were tapped in a later stage of
818 the eruption. However, the crustal heating hypothesis is not consistent with our xenolith
819 data because of the following reasons. First, the consistency of equilibration temperatures
820 estimated from the glass and xenolith mineralogy supports coexistence of glass and
821 minerals in the xenoliths at a mantle depth (Takahashi, 1986). Second, our pressure
822 estimates using the pyroxene compositions at the outermost rim also negate any heating
823 events for glass-bearing samples in a crustal magma chamber. The occurrence of glass
824 exclusively in samples giving higher pressures clearly supports that the melt actually

formed in the mantle.

More consistent explanation of the stratigraphic control of the xenolith thermal history is xenolith extraction by single-stage magma transportation in the mantle and subsequent eruption. Xenoliths in the deep LAB zone were incorporated into magma earlier and traveled longer distances than those in the shallow lithospheric mantle, and thus separation and probably size sorting took place more effectively for xenoliths from the deep LAB zone than those from the shallow lithospheric mantle. Such relations between depth and timing of xenolith entrapment in the ascending magma and sorting effect lead to the earlier exhumation of shallow mantle followed by deeper mantle materials, which is consistent with the systematic stratigraphic occurrence of the xenolith types.

Reconstruction of LAB zone in the mantle beneath Ichinomegata

Our pressure estimation allows us to clarify the depth variations of the diversity of the mantle beneath Ichinomegata as documented by previous studies (e.g., Takahashi, 1980, 1986; Arai et al., 2007) (Figs. 7 and 8). Thermal, rheological, and chemical LAB zones beneath Ichinomegata are inferred in this section on the basis of depth variation of temperature, microstructure, and mineral chemistry shown in Figures 7, 8, and 9 and

842 summarized in Table 5. These structures are compared with the well-documented structures
843 of the LAB zone of cratonic mantle using xenolith samples to characterize LAB zone
844 beneath Ichinomegata in an arc environment. Then, the origin of the LAB zone beneath
845 Ichinomegata is discussed.
846
847 **Thermal LAB zone**
848 Although previous studies (Takahashi, 1986; Kushiro, 1987) depicted thermal structures
849 based mainly on petrology and thermometry of mafic rocks, they are qualitative and did not
850 fully utilize information from peridotite xenoliths. Our thermal structure is quantitative on
851 the basis of information taken directly from the mantle. The estimated overall thermal
852 gradient shortly before the xenolith extraction is as steep as 10 K/km, which suggests a
853 thermal boundary layer in the LAB zone beneath Ichinomegata at 28-55 km depth. Such
854 steep xenolith geotherms are reported from the deepest part of SCLM, though its origin is
855 controversial (e.g., Boyd, 1973; O'Reilly and Griffin, 2010) and the temperature is
856 considerably higher (~1400 °C; Boyd, 1973) than beneath Ichinomegata (~1100 °C).
857 Takahashi (1980) revealed that half of the peridotite xenoliths from Ichinomegata
858 underwent a heating event shortly before the xenolith extraction and that the remaining half

859 did not. He, however, attributed the remarkable difference in thermal history to a local
860 effect by magmas passing through the mantle without specifying the depth of the heating
861 event. We clarified that a heating event took place at depths greater than ~45 km (Table 5),
862 which strongly supports that the heating took place near the LAB induced by
863 asthenospheric upwelling on the spatial scale much greater than that assumed by Takahashi
864 (1986).
865
866 **Rheological LAB zone**
867 The shallow mantle composed of granular peridotites is underlain by that of
868 porphyroclastic peridotites beneath Ichinomegata (Fig. 8; Table 5). The depth variation of
869 microstructure supports a rheological stratification with increasing shear strain with depth.
870 Satsukawa and Michibayashi (2014) argued that the strain decreased with depth, which
871 is inconsistent with our results. They applied a geothermobarometer of Brey and Köhler
872 (1990) to CaO contents of orthopyroxene assuming 1.0 GPa pressure and obtained fairly
873 scattered temperatures for each sample covering the entire range of our estimates
874 (800-1100 °C). The large scatter is due to the CaO zoning in orthopyroxene (Fig. 3). They
875 estimated the relative depths from the variation of minimum temperatures, which are

876 assumed to have a positive correlation with pressures. They adopted the minimum
877 temperatures because lower temperatures are commonly preserved at the rim recording
878 conditions closer to the surrounding environment than the core does. Such zoning pattern is,
879 however, not the case in Ichinomegata except for Type O1 (Fig. 3). Thus, their argument
880 that the shallower mantle was more strained which was based on the negative correlation of
881 the minimum temperature and the strength of crystallographic preferred orientation is
882 irreconcilable with our data. The most deformed sample (I708) in Satsukawa and
883 Michibayashi (2014) is a symplectite-free spinel peridotite, which is unique in that the
884 other samples are symplectite-bearing plagioclase peridotites. According to our results, the
885 unique xenolith is inferred to have been derived from a depth deeper than the other
886 xenoliths studied by them. This is consistent with our contention that the deeper mantle is
887 more strained than the shallower mantle beneath Ichinomegata.

888 Similar microstructural stratification, indicating increasing deformation with depth, is
889 reported from the SCLM (e.g., Boyd, 1973; Ehrenberg, 1979; Kopylova et al., 1999;
890 Agashev et al., 2013). Such transition in microstructure may correspond to the conceptually
891 presumed rheological boundary layer between the rigid lithosphere and the ductile and
892 convective asthenosphere (e.g., Sleep, 2005, 2006). The depths of the transition in the root

of SCLM are as deep as 170-220 km (O'Reilly and Griffin, 2010; Agashev et al., 2013). By contrast, the boundary layer in the LAB zone beneath Ichinomegata is as shallow as 40-60 km.

Chemical LAB zone

The chemical stratification of the mantle beneath Ichinomegata is unclear in terms of major element chemistry of olivine such as Mg# (Fig. 8). This is different from the case at the root of SCLM, where the clear decrease in the Mg# of olivine is the common feature (Griffin et al., 2003; O'Reilly and Griffin, 2006, 2010). The more oxidized environment in the deeper levels beneath Ichinomegata is suggested, which is opposite to the case found at the root of SCLM (Frost and McCammon, 2008).

More clear evidence for chemical stratification in the mantle beneath Ichinomegata is provided by previous geochemical studies. Tanaka and Aoki (1981) reported whole-rock REE patterns of peridotite xenoliths and those of clinopyroxene in them. Later, Abe et al. (1998) also reported REE patterns of the clinopyroxene from various lithologies, and Satsukawa et al. (2017) reported REE patterns of clinopyroxene from plagioclase lherzolites. Their REE patterns of plagioclase and/or symplectite- and amphibole-bearing

peridotites are characterized by LREE depletion and near chondritic whole-rock middle rare earth element (MREE) and heavy rare earth element (HREE) abundances. By contrast, those of amphibole and symplectite-absent spinel peridotite are characterized by slight LREE enrichment and depletion of MREE and HREE. Combining the contrasting mineral assemblages and our depth estimation allow estimation of geochemical stratification with regard to REE abundances beneath Ichinomegata; the shallow layer shows REE pattern akin to that of the source mantle of mid-ocean ridge basalt (MORB) and the deeper layer is enriched in LREE with depleted HREE.

Discussion

Formation condition of LAB zone beneath Ichinomegata

Defining mechanism of LAB proposed so far is dry lithospheric mantle (<0.01 wt.% H_2O) underlain by either subsolidus H_2O-bearing asthenosphere (e.g., Chu and Korenaga, 2012), asthenosphere having smaller grain size (e.g., Karato, 2012), or super-solidus asthenosphere (Hirschmann, 2010). The common condition of these models is the absence of hydrous phases, either hydrous minerals or H_2O-rich fluid phase, irrespective of oceanic (Hirth and Koheldstedt, 1996) or continental environment (Wang, 2010). The LAB zone

including lithospheric mantle beneath Ichinomegata is pervasively hydrated, requiring another mechanism of LAB formation. We propose that the thermal structure and wet solidus control LAB depth: peridotites with H_2O-rich fluid and hydrous phases such as amphibole consist of the lithosphere and peridotites with hydrous melt consist of the uppermost asthenosphere (Green et al., 2010). We speculate that this could be one of the important mechanisms for LAB formation in arc settings. The important question is if such LAB zone involving highly mobile H_2O-rich fluid and hydrous melt can be viewed as at a steady state or if it is a snapshot of dynamically developing LAB zone.

A major difference between lithospheric mantle in the arc and continental settings is the presence of significant amounts of water in the former (0.1-1.0 vs. < 0.01 wt.% H_2O; Kelley et al., 2006; Wang, 2010). Water is stored in amphibole, phlogopite (Abe et al., 1992) and fluid phase in the shallow levels beneath Ichinomegata (28-41 km), though it should be noted that the shallowest sample (HK64081206g) lacks microstructures indicating the presence of fluid phase (Table 1) and, thus, may be undersaturated in water. By contrast, water is stored in the melt phase in the deep levels (45-55 km). The melt is distributed inhomogeneously and forms pockets in pyroxene-rich layers, suggesting that the microstructures were far from textural equilibrium (e.g., Waff and Bulau, 1979; Holness et

al., 2005, 2012). This is possibly a reason for maintaining as high as 2 vol. % of melt in the glass-bearing samples. The water content of such melt is estimated to be ~2-5 wt.% based on weight deficiency of glass in the EPMA analyses, which is below the water saturation under the estimated pressure and temperature conditions (>12 wt.% at 1020 °C and 1.2 GPa; Grove et al., 2006). Vesicles present in glass (Fig. 3c) suggest degassing during xenolith extraction, which could have decreased the water content. The temperatures estimated from the glass compositions using eq. (15) of Putirka (2008) assuming the water contents of ~2-5 wt.% are consistent with the derivation temperatures of the examined xenoliths. If we assume the water content of ~12 wt.%, which corresponds to the value of water saturation (Grove et al., 2006), the thermometer gives very low temperatures ranging 949-984 °C. These values are significantly lower than the xenolith derivation temperatures. Therefore, we argue that the original water content of melt was close to ~2-5 wt.% and vesiculation did not affect the water content of the glass. Combining this with the absence of amphibole and fluid in peridotites from the deeper levels, we conclude that the deeper samples were H_2O-undersaturated in the mantle before the xenolith extraction. The drastic change of water carriers beneath Ichinomegata, the water undersaturation of the shallowest plagioclase lherzolite (~0.7 GPa), LREE-depleted REE patterns with positive anomalies of

961 Th and U of the shallower samples and flat or LREE-enriched REE patterns of the deeper
962 samples (Tanaka and Aoki, 1981; Abe et al. 1998; Satsukawa et al., 2017), and
963 inhomogeneous distribution of melt phase as pockets all suggest that H_2O was supplied
964 from underlying asthenosphere up to the depth of ~30 km before the xenolith extraction
965 and that the process caused a decrease in the depth of the LAB zone. Water might have
966 been transported to the LAB zone through fractures or other fast transportation paths at
967 least in the shallower level before the asthenosphere upwelling. The presence of such fast
968 transportation paths is supported by the occurrence of amphibole-rich veins and
969 amphibole-rich peridotite lithology among Ichinomegata xenoliths (Abe et al., 1992).
970 Another important dynamic aspect of the LAB beneath Ichinomegata is a temporal
971 change of thermal structure, which is expected in the LAB zone, where the mechanism of
972 heat transfer changes from convection to conduction. Takahashi (1980, 1986) found that
973 half of the Ichinomegata peridotite xenoliths show evidence of prolonged heating for more
974 than one thousand years (minimum time scale). He attributed the heat source to that
975 released from magmas generated in the asthenosphere. Our barometry and depth-dependent
976 thermal history: simple cooling in the shallower layer and cooling followed by heating in
977 the deeper layer (Table 5) clearly demonstrate that heat source was actually in the

978 asthenosphere, which upwelled just before the xenolith extraction and generated basaltic
979 magma for the Ichinomegata volcanism. Heat might be effectively transported either by
980 basaltic magma generated in the upwelling asthenosphere or by extensive thermochemical
981 thinning of the lithosphere, both of which account for the short timescales of a heating
982 event.

983 All these depth dependent systematics characterizing the mantle beneath Ichinomegata
984 strongly suggest that the identified LAB zone is dynamically evolving rather than at a
985 steady state. We infer that the LAB zone beneath Ichinomegata is a dynamic entity and
986 became shallower with time driven by heat and material transportation from the underlying
987 asthenosphere.

988 One of the most important points in our study is that the sample-derived wet solidus at
989 ~40 km depth coincides with the transition of microstructures from granular to
990 porphyroclastic textures with increasing depth. The depth range of samples showing
991 porphyroclastic texture (41-52 km) roughly overlaps with that of the presence of melt, and
992 the depth range of samples with granular texture (28-32 km) overlaps with that of the
993 presence of H_2O-rich fluid phase. The coincidence of the depth-dependent transitions of
994 microstructure and phase assemblage strongly suggests that melting might have governed

995 the rheological transition. We propose that wet solidus and thermal structure control the
996 upper depth limit of the rheological boundary layer beneath Ichinomegata. This has
997 important implications for the generation of magma in an arc wedge mantle.
998
999 **Implication**
1000 The depth variations of diverse properties of the mantle beneath Ichinomegata based on
1001 our geobarometry of peridotite xenoliths show that the depth of the LAB zone beneath
1002 Ichinomegata is 40-60 km and controlled by the thermal structure and wet solidus. The
1003 mean depth of LAB beneath the Japan Sea is estimated to be 60 km by shear-wave
1004 tomography studies (Yoshizawa et al., 2010; Zheng et al., 2011), which tends to decrease
1005 towards the Northeast Japan arc. Several studies of seismic structures of the wedge mantle
1006 beneath the Northeast Japan arc show that the lithospheric mantle beneath the volcanic arc,
1007 where the MOHO is 35 km deep, is very thin or even absent (Zhao et al., 1992; Nakajima
1008 and Hasegawa, 2003; Nakajima et al., 2005; Yoshizawa et al., 2010). If these results are
1009 combined with our study, the depth of the LAB zone across Northeast Japan decreases from
1010 ~60 km beneath Japan Sea to <40 km beneath the volcanic front (Fig. 10).
1011 Nakajima and Hasegawa (2003) estimated the temperature of the uppermost mantle

(asthenosphere or LAB zone at ~40 km) beneath the volcanic front of Northeast Japan as 1000-1130 °C and that beneath the back-arc side as 960-1090 °C based on seismic attenuation data. They used 1025 °C at a 40 km depth, which was roughly estimated from petrologic studies of Ichinomegata xenoliths (Aoki, 1987; Kushiro, 1987; Takahashi, 1986), as reference conditions for the thermal structure. Our accurate geobarometry on the Ichinomegata samples (e.g., IC81-5; 1016 °C at 41 km) is fortunately very close to the reference conditions. Tatsumi et al. (1983) proposed deepening of isotherm in the wedge mantle of Northeast Japan arc towards the back-arc side on the basis of across-arc variation of experimentally estimated magma segregation depth. Kuritani et al. (2014a) estimated the conditions of magma generation (temperature, pressure, degree of melting, and water content) for Sannomegata basalt by applying multi-component thermodynamics to the basaltic scoriae. The estimated melting conditions for Sannomegata are 1220-1230 °C in temperature, ~1.8 GPa in pressure, and ~7 % in degree of melting (Fig. 10). Kuritani et al. (2014a, 2014b) also estimated the conditions of magma generation for the lava from Iwate volcano, occurring to the east of Ichinomegata at the volcanic front. The estimated melting conditions for Iwate volcano are ~1250 °C in temperature, ~1.3 GPa in pressure, and ~15 % in melting degree. These geophysical and petrologic estimates support that the

asthenosphere beneath the northeast Japan arc at a given depth becomes cooler with the distance from the volcanic front towards the back-arc side.

There are several lines of geophysical evidence for decreasing geothermal gradient of the lithosphere from the volcanic front towards the back-arc side. They are surface heat flow, Curie point depth at which the crustal temperature reaches the Curie point of magnetic minerals, and depth of seismic-aseismic boundary across which behavior of crustal materials changes from brittle to ductile. Tanaka et al. (2004) compiled heat flow data of Japan and showed that the heat flow in the volcanic front is significantly higher than that in the back-arc side in Northeast Japan. Okubo et al. (1994) revealed that the Curie point depth of Northeast Japan slightly increases from the volcanic front to back-arc. Nakajima et al. (2001) compiled the earthquake focal depth in Northeast Japan and showed a deepening tendency of the lower bound from the volcanic front to back-arc suggesting decreasing geothermal gradient towards the back-arc side (McKenzie et al., 2016).

We have shown that the wet solidus and thermal structure determine the depth of the upper limit of the LAB zone beneath Ichinomegata. If this formation condition of LAB is generalized, the decreasing depth of LAB from the back-arc side to the volcanic front is consistently explained by increasing temperature of the asthenosphere and increasing

1046 geothermal gradient of the lithosphere in the Northeast Japan arc (Fig. 10). The wet solidus
1047 has a very large or even negative dP/dT at pressures lower than ~2 GPa, which is
1048 contrasting to a smaller and positive dP/dT for the dry solidus. Because of this, a hotter
1049 thermal profile of lithosphere and asthenosphere crosses the wet solidus at a lower pressure
1050 but at a similar temperature (Fig. 10b). Consequently, under water-saturated conditions, the
1051 mantle beneath the volcanic front at higher temperature melts at a lower pressure than that
1052 beneath the back-arc side, which results in the shallowing the LAB zone toward the
1053 volcanic front. It should be noted that the melting temperatures are similar irrespective of
1054 the thermal profile (Fig. 10).

1055 The variation of LAB depth and its temperature may play an important role in
1056 controlling the depth of melt generation and segregation beneath the Northeast Japan arc
1057 (Kuno and Aoki, 1970; Tatsumi et al., 1983; Takahashi, 1986; Kushiro, 1987, Kimura and
1058 Yoshida, 2006). Kuritani et al. (2014a, 2014b) quantified the essential feature of across-arc
1059 variations for the northeast Japan arc; deepening magma generation and segregation as well
1060 as decreasing melting degree towards the back arc side at a similar temperature (Kuritani et
1061 al., 2014a, 2014b). The melting condition for Sannomegata basalt, active ~20 ka (Kitamura,
1062 1990), does not lie on the extension of the geotherm derived from Ichinomegata xenoliths,

1063 erupted 60-80 ka and is higher by ~100 °C than the geotherm at ~60 km depth (Fig. 10;
1064 Kuritani et al., 2014a). There is a similar relationship between the magma generation
1065 condition of Iwate volcano (Kuritani et al., 2014a) and the geotherm that we inferred for
1066 beneath the volcanic front (Fig. 10). These relationships are explained by either heat
1067 (and/or material)-fluxed melting or decompressional melting. If fluxed melting was
1068 dominant, we may argue that it took ~50 thousand years to increase the temperature by
1069 100 °C before the magma generation for the Sannomegata volcanism (① in Fig. 10). If
1070 decompressional melting was a dominant melting mechanism, we may argue that deeply
1071 resided mantle ascended to a shallower asthenosphere to induce partial melting and melt
1072 segregation (② in Fig. 10). The potential temperature (T_p) of the mantle can be estimated
1073 to be ~1250 °C by finding an intersection of the melting adiabat for Sannomegata magma
1074 and extrapolation of the Ichinomegata geotherm. This T_p is significantly lower than that for
1075 MORB (Herzberg et al., 2007; Putirka et al., 2007) and back-arc basin basalt (Wiens et al.,
1076 2006), and is lower than T_p for basalts from northeast Japan arc (Tatsumi et al., 1983,
1077 1994).
1078
1079 **Acknowledgments**

The authors are grateful to Dr. Dan McKenzie for fruitful discussions and suggestions, Dr. T. Koyaguchi of the University of Tokyo for critical discussions, Drs. T. Iizuka and S. Wallis of the University of Tokyo for helpful discussions, and H. Yoshida for help in EPMA analyses at The University of Tokyo. We also acknowledge the constructive reviews of Eiichi Takahashi and an anonymous reviewer as well as the editorial handling and comments by Dr. Heather Handley. This study was supported by JSPS KAKENHI Grant Number 17H02982.

References

Abe, S., and Yamamoto, M. (1999) Rb-Sr mineral isochron ages of mantle peridotite xenoliths from Ichinomegata and Kurose, Japan. Journal of Mineralogy, Petrology and Economic Geology, 94, 295-310 (in Japanese with an English abstract).

Abe, N., Arai, S., and Saeki, Y. (1992) Hydration processes in the arc mantle; petrology of the Megata peridotite xenoliths, the Northeast Japan arc. Journal of Mineralogy, Petrology and Economic Geology, 87, 305-317 (in Japanese with an English abstract).

1096 Abe, N., Arai, S., and Yurimoto, H. (1998) Geochemical characteristics of the uppermost
1097 mantle beneath the Japan island arcs: implications for upper mantle evolution.
1098 Physics of the Earth and Planetary Interiors, 107, 233-248.
1099 Agashev, A.M., Ionov, D.A., Pokhilenko, N.P., Golovin, A.V., Cherepanova, Y., and
1100 Sharygin, I.S. (2013) Metasomatism in lithospheric mantle roots: Constraints from
1101 whole-rock and mineral chemical composition of deformed peridotite xenoliths from
1102 kimberlite pipe Udachnaya. Lithos, 160, 201-215.
1103 Anderson, D.L. (1995) Lithosphere, asthenosphere, and perisphere. Reviews of Geophysics,
1104 33, 125-149.
1105 Aoki, K. (1971) Petrology of mafic inclusions from Itinome-gata, Japan. Contributions to
1106 Mineralogy and Petrology, 30, 314-331.
1107 Aoki, K. (1987) Japanese Island arc: xenoliths in alkali basalts, high-alumina basalts, and
1108 calc-alkaline andesites and dacites. In P.H., Nixon, Ed., Mantle Xenoliths, p. 319-333.
1109 Wiley, NewYork.
1110 Aoki, K. and Shiba, I. (1973) Pargasites in lherzolite and websterite inclusions from
1111 Itinome-gata, Japan. The Journal of the Japanese Association of Mineralogists,
1112 Petrologists and Economic Geologists, 68, 303-310.

1113 Aoki, K. and Shiba, I. (1974) Olivines from lherzolite inclusions of Itinome-gata, Japan.
1114 Memories of the Geological Society of Japan, 11, 1-10.
1115 Arai, S. (1994) Characterization of spinel peridotites by olivine-spinel compositional
1116 relationships: review and interpretation. Chemical geology, 113, 191-204.
1117 Arai, S., Abe, N., and Ishimaru, S. (2007) Mantle peridotites from the Western Pacific.
1118 Gondwana Research, 11, 180-199.
1119 Ballhaus, C., Berry, R.F., and Green, D.H. (1991) High pressure experimental calibration of
1120 the olivine-orthopyroxene-spinel oxygen geobarometer: implications for the
1121 oxidation state of the upper mantle. Contributions to Mineralogy and Petrology, 107,
1122 27-40.
1123 Behr, W.M., and Hirth, G. (2014) Rheological properties of the mantle lid beneath the
1124 Mojave region in southern California. Earth and Planetary Science Letters, 393,
1125 60-72.
1126 Bertrand, P., and Mercier, J.C.C. (1985) The mutual solubility of coexisting ortho-and
1127 clinopyroxene: toward an absolute geothermometer for the natural system?. Earth and
1128 Planetary Science Letters, 76, 109-122.

1129 Borghini, G., Fumagalli, P., and Rampone, E. (2010) The stability of plagioclase in the
1130 upper mantle: subsolidus experiments on fertile and depleted lherzolite. Journal of
1131 Petrology, 51, 229-254.
1132 Boyd, F.R. (1973) A pyroxene geotherm. Geochimica et Cosmochimica Acta, 37,
1133 2533-2546.
1134 Brady, J.B., and MacCallister, R.H. (1983) Diffusion data for clinopyroxenes from
1135 homogenization and self-diffusion experiments. American Mineralogist, 68, 95-105.
1136 Brandon, A.D., Creaser, R.A., Shirey, S.B., and Carlson, R.W. (1996) Osmium recycling in
1137 subduction zones. Science, 272, 861-863.
1138 Brey, G.P., and Köhler, T. (1990) Geothermobarometry in four-phase lherzolites II. New
1139 thermobarometers, and practical assessment of existing thermobarometers. Journal of
1140 Petrology, 31, 1353-1378.
1141 Chakraborty, S. (2010) Diffusion coefficients in olivine, wadsleyite and ringwoodite.
1142 Reviews in mineralogy and geochemistry, 72, 603-639.
1143 Cherniak, D.J., and Dimanov, A. (2010) Diffusion in pyroxene, mica and amphibole.
1144 Reviews in Mineralogy and Geochemistry, 72, 641-690.

1145 Chu, X., and Korenaga, J. (2012) Olivine rheology, shear stress, and grain growth in the
1146 lithospheric mantle: Geological constraints from the Kaapvaal craton. Earth and
1147 Planetary Science Letters, 333, 52-62.
1148 Dimanov, A., and Sautter, V. (2000) "Average" interdiffusion of (Fe, Mn)-Mg in natural
1149 diopside. European Journal of Mineralogy, 12, 749-760.
1150 Ehrenberg, S.N. (1979) Garnetiferous ultramafic inclusions in minette from the Navajo
1151 volcanic field. In F.R. Boyd and H.O.A. Meyer Ed., The Mantle Sample: Inclusion in
1152 Kimberlites and Other Volcanics, Volume 16, p. 330-344.
1153 Fabriès, J. (1979) Spinel-olivine geothermometry in peridotites from ultramafic complexes.
1154 Contributions to Mineralogy and Petrology, 69, 329-336.
1155 Fischer, K.M., Ford, H.A., Abt, D.L., and Rychert, C.A. (2010) The
1156 lithosphere-asthenosphere boundary. Annual Review of Earth and Planetary Sciences,
1157 38, 551-575.
1158 Frost, D.J., and McCammon, C.A. (2008) The redox state of Earth's mantle. Annual
1159 Review of Earth and Planetary Sciences, 36, 389-420.
1160 Fumagalli, P., Borghini, G., Rampone, and E., Poli, S. (2017) Experimental calibration of
1161 Forsterite-Anorthite-Ca-Tschermak-Enstatite (FACE) geobarometer for mantle

1162 peridotites. Contributions to Mineralogy and Petrology, 172, 19, doi:
1163 10.1007/s00410-017-1352-2.

1164 Ganguly, J., Ito, M., and Zhang, X. (2007) Cr diffusion in orthopyroxene: Experimental
1165 determination, ^{53}Mn-^{53}Cr thermochronology, and planetary applications. Geochimica
1166 et Cosmochimica Acta, 71, 3915-3925.

1167 Gasparik, T. (2003) Phase diagrams for geoscientists. An Atlas of the Earth's Interior, 462 p.
1168 Springer Ed.

1169 Green, D.H. (1973) Experimental melting studies on a model upper mantle composition at
1170 high pressure under water-saturated and water-undersaturated conditions. Earth and
1171 Planetary Science Letters, 19, 37-53.

1172 Green, D.H., Hibberson, W.O., Kovács, I., and Rosenthal, A. (2010) Water and its influence
1173 on the lithosphere-asthenosphere boundary. Nature, 467, 448-451.

1174 Griffin, W.L., Doyle, B.J., Ryan, C.G., Pearson, N.J., O'Reilly, S.Y., Davies, R., Kivi, K.,
1175 Van Achterbergh, E., and Natapov, L.M. (1999) Layered mantle lithosphere in the
1176 Lac de Gras area, Slave craton: composition, structure and origin. Journal of
1177 Petrology, 40, 705-727.

1178 Griffin, W.L., O'Reilly, S.Y., Natapov, L.M., and Ryan, C.G. (2003) The evolution of
1179 lithospheric mantle beneath the Kalahari Craton and its margins. Lithos, 71, 215-241.
1180 Grove, T.L., Chatterjee, N., Parman, S.W., and Médard, E. (2006) The influence of H_2O on
1181 mantle wedge melting. Earth and Planetary Science Letters, 249, 74-89.
1182 Hayashi, H. (1955). Volcanic ejecta around Ichinomegata, Oga peninsula, Akita prefecture.
1183 Journal of Geological Society of Japan, 61, 240-248 (in Japanese with a French
1184 abstract).
1185 Harigane, Y., Mizukami, T., Morishita, T., Michibayashi, K., Abe, N., and Hirano, N.
1186 (2011) Direct evidence for upper mantle structure in the NW Pacific Plate:
1187 Microstructural analysis of a petit-spot peridotite xenolith. Earth and Planetary
1188 Science Letters, 302, 194-202.
1189 Herzberg, C., Asimow, P.D., Arndt, N., Niu, Y., Lesher, C.M., Fitton, J.G., Cheadle, M.J.,
1190 and Saunders, A.D. (2007) Temperatures in ambient mantle and plumes: Constraints
1191 from basalts, picrites, and komatiites. Geochemistry, Geophysics, Geosystems, 8, 34,
1192 doi:10.1029/2006GC001390.

1193 Hirschmann, M.M. (2000) Mantle solidus: Experimental constraints and the effects of
1194 peridotite composition. Geochemistry, Geophysics, Geosystems, 1, 26,
1195 doi:10.1029/2000GC000070.
1196 Hirschmann, M.M. (2010) Partial melt in the oceanic low velocity zone. Physics of the
1197 Earth and Planetary Interiors, 179, 60-71.
1198 Hirth, G., and Kohlstedt, D.L. (1996) Water in the oceanic upper mantle: implications for
1199 rheology, melt extraction and the evolution of the lithosphere. Earth and Planetary
1200 Science Letters, 144, 93-108.
1201 Holness, M.B., Cheadle, M.J., and McKenzie, D. (2005) On the use of changes in dihedral
1202 angle to decode late-stage textural evolution in cumulates. Journal of Petrology, 46,
1203 1565-1583.
1204 Holness, M.B., Humphreys, M.C., Sides, R., Helz, R.T., and Tegner, C. (2012) Toward an
1205 understanding of disequilibrium dihedral angles in mafic rocks. Journal of
1206 Geophysical Research: Solid Earth, 117, 31, doi:10.1029/2011JB008902.
1207 Iwasaki, T., Levin, V., Nikulin, A., and Iidaka, T. (2013) Constraints on the Moho in Japan
1208 and Kamchatka. Tectonophysics, 609, 184-201.

1209 Jaques, A.L., and Green, D.H. (1980) Anhydrous melting of peridotite at 0-15 kb pressure
1210 and the genesis of tholeiitic basalts. Contributions to mineralogy and petrology, 73,
1211 287-310.
1212 Karato, S. (2010) Rheology of the deep upper mantle and its implications for the
1213 preservation of the continental roots: A review. Tectonophysics, 481, 82-98.
1214 Karato, S. (2012) On the origin of the asthenosphere. Earth and Planetary Science Letters,
1215 321, 95-103.
1216 Katsui, Y., Yamamoto, M., Nemoto, S., and Niida, K. (1979) Genesis of Calc-Alkalic
1217 Andesites from Oshima-Ōshima and Ichinomegata Volcanoes, North Japan. Journal
1218 of the Faculty of Science, Hokkaido University. Series 4, Geology and Mineralogy,
1219 19, 157-168.
1220 Kawasaki, T., and Ito, E. (1994) An experimental determination of the exchange reaction of
1221 Fe^{2+} and Mg^{2+} between olivine and Ca-rich clinopyroxene. American Mineralogist,
1222 79, 461-477.
1223 Kelley, K.A., Plank, T., Grove, T.L., Stolper, E.M., Newman, S., and Hauri, E. (2006)
1224 Mantle melting as a function of water content beneath back-arc basins. Journal of
1225 Geophysical Research: Solid Earth, 111, 27, doi:10.1029/2005JB003732.

1226 Kimura, J., and Yoshida, T. (2006) Contributions of slab fluid, mantle wedge and crust to
1227 the origin of Quaternary lavas in the NE Japan arc. Journal of Petrology, 47,
1228 2185-2232.
1229 Kitamura, S. (1990) Ages of Megata maars in the Oga peninsula, Japan. Annals of The
1230 Tohoku Geographycal Asocciation, 42, 161-167 (in Japanese).
1231 Klemme, S., and O'Neill, H.S. (2000) The effect of Cr on the solubility of Al in
1232 orthopyroxene: experiments and thermodynamic modelling. Contributions to
1233 Mineralogy and Petrology, 140, 84-98.
1234 Kopylova, M.G., Russell, J.K., and Cookenboo, H. (1999) Petrology of peridotite and
1235 pyroxenite xenoliths from the Jericho kimberlite: implications for the thermal state of
1236 the mantle beneath the Slave craton, northern Canada. Journal of Petrology, 40,
1237 79-104.
1238 Koyaguchi, T. (1986) Life-time of a stratified magma chamber recorded in ultramafic
1239 xenoliths from Ichinomegata volcano, northeastern Japan. Bulletin of Volcanology,
1240 48, 313-323.

Kumagai, Y., Kawamoto, T., and Yamamoto, J. (2014) Evolution of carbon dioxide-bearing saline fluids in the mantle wedge beneath the northeast Japan Arc. Contributions to Mineralogy and Petrology, 168, 1-13.

Kuno, H. (1967). Mafic and ultramafic nodules from Itinome-gata Japan. In P.J. Wyllie, Ed., Ultramafic and related rocks, p. 337-342. John Wiley, New York.

Kuno, H., and Aoki, K. (1970) Chemistry of ultramafic nodules and their bearing on the origin of basaltic magmas. Physics of the Earth and Planetary Interiors, 3, 273-301.

Kuritani, T., Yoshida, T., Kimura, J., Takahashi, T., Hirahara, Y., Miyazaki, T., Senda, R., Chang, Q., and Ito, Y. (2014a) Primary melt from Sannome-gata volcano, NE Japan arc: constraints on generation conditions of rear-arc magmas. Contributions to Mineralogy and Petrology, 167, 969.

Kuritani, T., Yoshida, T., Kimura, J., Hirahara, Y., and Takahashi, T. (2014b) Water content of primitive low-K tholeiitic basalt magma from Iwate Volcano, NE Japan arc: implications for differentiation mechanism of frontal-arc basalt magmas. Mineralogy and Petrology, 108, 1-11.

1256 Kushiro, I. (1987) A petrological model of the mantle wedge and lower crust in the
1257 Japanese island arcs. In B.O. Mysen, Ed., Magmatic processes: physicochemical
1258 principles, p. 165-181. Geochemical Society, Washington, D.C.
1259 Leake, B.E., Woolley, A.R., Arps, C.E.S., Birch, W.D., Gilbert, M.C., Grice, J.D.,
1260 Hawthorne, F.C., Kato, A., Kish, H.J., Krivovichev, V.G., and others. (1997)
1261 Nomenclature of amphiboles; report of the subcommittee on amphiboles of the
1262 International Mineralogical Association Commission on New Minerals and Mineral
1263 Names. The Canadian Mineralogist, 35, 219-246.
1264 Lindsley, D.H. (1983) Pyroxene thermometry. American Mineralogist, 68, 477-493.
1265 McKenzie, D., and Bickle, M.J. (1988) The volume and composition of melt generated by
1266 extension of the lithosphere. Journal of Petrology, 29, 625-679.
1267 McKenzie, D., Jackson, J. and Priestley, K. (2016) Thermal structure of oceanic and
1268 continental lithosphere. Earth and Planetary Science Letters, 233, 337-349.
1269 Mercier, J.C.C., Benoit, V., and Girardeau, J. (1984) Equilibrium state of diopside-bearing
1270 harzburgites from ophiolites: geobarometric and geodynamic implications.
1271 Contributions to Mineralogy and Petrology, 85, 391-403.
1272 Mysen, B.O., and Boettcher, A.L. (1975) Melting of a Hydrous Mantle: I. Phase Relations

of Natural Peridotite at High Pressures and Temperatures with Controlled Activities of Water, Carbon Dioxide, and Hydrogen. Journal of Petrology, 16, 520-548.

Nakajima, J., and Hasegawa, A. (2003) Estimation of thermal structure in the mantle wedge of northeastern Japan from seismic attenuation data. Geophysical Research Letters, 30, 4, doi:10.1029/2003GL017185.

Nakajima, J., Matsuzawa, T., Hasegawa, A., and Zhao, D. (2001) Three-dimensional structure of Vp, Vs, and Vp/Vs beneath northeastern Japan: Implications for arc magmatism and fluids. Journal of Geophysical Research: Solid Earth, 106, 21843-21857.

Nakajima, J., Takei, Y., and Hasegawa, A. (2005) Quantitative analysis of the inclined low-velocity zone in the mantle wedge of northeastern Japan: A systematic change of melt-filled pore shapes with depth and its implications for melt migration. Earth and Planetary Science Letters, 234, 59-70.

Nickel, K.G., and Brey, G. (1984) Subsolidus orthopyroxene-clinopyroxene systematics in the system CaO-MgO-SiO_2 to 60 kb: a re-evaluation of the regular solution model. Contributions to Mineralogy and Petrology, 87, 35-42.

1289 Niida, K., and Green, D.H. (1999) Stability and chemical composition of pargasitic
1290 amphibole in MORB pyrolite under upper mantle conditions. Contributions to
1291 Mineralogy and Petrology, 135, 18-40.
1292 Nixon P.H. (1987) Mantle Xenoliths, 844 p. Wiley, New York.
1293 Okubo, Y., and Matsunaga, T. (1994) Curie point depth in northeast Japan and its
1294 correlation with regional thermal structure and seismicity. Journal of Geophysical
1295 Research: Solid Earth, 99, 22363-22371.
1296 O'Reilly, S.Y., and Griffin, W.L. (1996) 4-D lithosphere mapping: methodology and
1297 examples. Tectonophysics, 262, 3-18.
1298 O'Reilly, S.Y., and Griffin, W.L. (2006) Imaging global chemical and thermal heterogeneity
1299 in the subcontinental lithospheric mantle with garnets and xenoliths: Geophysical
1300 implications. Tectonophysics, 416, 289-309.
1301 O'Reilly, S.Y., and Griffin, W.L. (2010) The continental lithosphere-asthenosphere
1302 boundary: can we sample it?. Lithos, 120, 1-13.
1303 O'Reilly, S.Y., Chen, D., Griffin, W.L., and Ryan, C.G. (1997) Minor elements in olivine
1304 from spinel lherzolite xenoliths: implications for thermobarometry. Mineralogical
1305 Magazine, 61, 257-269.

Ozawa, K. (1984) Olivine-spinel geospeedometry: Analysis of diffusion-controlled Mg-Fe^{2+} exchange. Geochimica et Cosmochimica Acta, 48, 2597-2611.

Ozawa, K., and Nagahara, H. (2000) Kinetics of diffusion-controlled evaporation of Fe-Mg olivine: Experimental study and implication for stability of Fe-rich olivine in the solar nebula. Geochimica et Cosmochimica Acta, 64, 939-955.

Ozawa, K., and Takahashi, N. (1995) PT history of a mantle diapir: the Horoman peridotite complex, Hokkaido, northern Japan. Contributions to Mineralogy and Petrology, 120, 223-248.

Ozawa, K., Nagahara, H., Morioka, M., Matsumoto, N., Hutcheon, I.D., Noguchi, T., and Kagi, H. (2012) Kinetics of evaporation of forsterite in vacuum. American Mineralogist, 97, 80-99.

Parkinson, I.J., and Arculus, R.J. (1999) The redox state of subduction zones: insights from arc-peridotites. Chemical Geology, 160, 409-423.

Putirka, K.D. (2008) Thermometers and barometers for volcanic systems. Reviews in Mineralogy and Geochemistry, 69, 61-120.

1321 Putirka, K.D., Perfit, M., Ryerson, F.J., and Jackson, M.G. (2007) Ambient and excess
1322 mantle temperatures, olivine thermometry, and active vs. passive upwelling.
1323 Chemical Geology, 241, 177-206.
1324 Sachtleben, T., and Seck, H.A. (1981) Chemical control of Al-solubility in orthopyroxene
1325 and its implications on pyroxene geothermometry. Contributions to Mineralogy and
1326 Petrology, 78, 157-165.
1327 Sakuyama, M., and Koyaguchi, T. (1984) Magma mixing in mantle xenolith-bearing
1328 calc-alkalic ejecta, Ichinomegata volcano, northeastern Japan. Journal of Volcanology
1329 and Geothermal Research, 22, 199-224.
1330 Sato, Y. and Ozawa, K. (2018) Dynamic processes in lithosphere-asthenosphere boundary
1331 zone; rheological structure from Ichinomegata mantle xenoliths. SIT28-11,
1332 Proceedings of Japan Geoscience Union Meeting, Makuhari.
1333 Satsukawa, T., and Michibayashi, K. (2014) Flow in the uppermost mantle during back-arc
1334 spreading revealed by Ichinomegata peridotite xenoliths, NE Japan. Lithos, 189,
1335 89-104.
1336 Satsukawa, T., Godard, M., Demouchy, S., Michibayashi, K., and Ildefonse, B. (2017).
1337 Chemical interactions in the subduction factory: New insights from an in situ trace

element and hydrogen study of the Ichinomegata and Oki-Dogo mantle xenoliths (Japan). Geochimica et Cosmochimica Acta, 208, 234-267.

Sautter, V., Jaoul, O., and Abel, F. (1988) Aluminum diffusion in diopside using the ^{27}Al (p, γ) ^{28}Si nuclear reaction: preliminary results. Earth and Planetary Science Letters, 89, 109-114.

Sleep, N.H. (2005) Evolution of the continental lithosphere. Annual Review of Earth and Planetary Sciences, 33, 369-393.

Sleep, N.H. (2006) Mantle plumes from top to bottom. Earth-Science Reviews, 77, 231-271.

Smith, D. (1999). Temperatures and pressures of mineral equilibration in peridotite xenoliths: review, discussion, and implications. In Y. Fei, C.M. Bertka and B.O. Mysen, Ed., Mantle petrology: field observations and high pressure experimentation: a tribute to Francis R.(Joe) Boyd, p. 171-188. Geochemical Society, Washington, D.C.

Smith, D., and Barron, B.R. (1991) Pyroxene-garnet equilibration during cooling in the mantle. American Mineralogist, 76, 1950-1963.

1354 Spera, F.J. (1984) Carbon dioxide in petrogenesis III: role of volatiles in the ascent of
1355 alkaline magma with special reference to xenolith-bearing mafic lavas. Contributions
1356 to Mineralogy and Petrology, 88, 217-232.
1357 Takahashi, E. (1980) Thermal history of lherzolite xenoliths-I. Petrology of lherzolite
1358 xenoliths from the Ichinomegata crater, Oga peninsula, northeast Japan. Geochimica
1359 et Cosmochimica Acta, 44, 1643-1658.
1360 Takahashi, E. (1986) Genesis of calc-alkali andesite magma in a hydrous mantle-crust
1361 boundary: Petrology of lherzolite xenoliths from the Ichinomegata crater, Oga
1362 peninsula, northeast Japan, part II. Journal of Volcanology and Geothermal Research,
1363 29, 355-395.
1364 Tanaka, A., Yamano, M., Yano, Y., and Sasada, M., (2004) Geothermal Gradient and Heat
1365 Flow Data in and around Japan, Digital Geoscience Map DGM P-5, Geological
1366 Survey of Japan.
1367 Tanaka, T., and Aoki, K. (1981). Petrogenic implications of REE and Ba data on mafic and
1368 ultramafic inclusions from Itinome-gata, Japan. The Journal of Geology, 89, 369-390.

1369 Tatsumi, Y., Furukawa, Y., and Yamashita, S. (1994) Thermal and geochemical evolution of
1370 the mantle wedge in the northeast Japan arc: 1. Contribution from experimental
1371 petrology. Journal of Geophysical Research: Solid Earth, 99, 22275-22283.
1372 Tatsumi, Y., Sakuyama, M., Fukuyama, H., and Kushiro, I. (1983) Generation of arc basalt
1373 magmas and thermal structure of the mantle wedge in subduction zones. Journal of
1374 Geophysical Research: Solid Earth, 88, 5815-5825.
1375 Titus, S.J., Medaris, L.G., Wang, H.F., and Tikoff, B. (2007) Continuation of the San
1376 Andreas fault system into the upper mantle: evidence from spinel peridotite xenoliths
1377 in the Coyote Lake basalt, central California. Tectonophysics, 429, 1-20.
1378 Van Orman, J.A., and Crispin, K.L. (2010) Diffusion in oxides. Reviews in Mineralogy and
1379 Geochemistry, 72, 757-825.
1380 von Seckendorff, V., and O'Neill, H.S.C. (1993) An experimental study of Fe-Mg
1381 partitioning between olivine and orthopyroxene at 1173, 1273 and 1423 K and 1.6
1382 GPa. Contributions to Mineralogy and Petrology, 113, 196-207.
1383 Waff, H.S., and Bulau, J.R. (1979) Equilibrium fluid distribution in an ultramafic partial
1384 melt under hydrostatic stress conditions. Journal of Geophysical Research: Solid
1385 Earth, 84, 6109-6114.

1386 Wallace, M.E., and Green, D.H. (1991) The effect of bulk rock composition on the stability
1387 of amphibole in the upper mantle: implications for solidus positions and mantle
1388 metasomatism. Mineralogy and Petrology, 44, 1-19.
1389 Wang, Q. (2010) A review of water contents and ductile deformation mechanisms of
1390 olivine: implications for the lithosphere-asthenosphere boundary of continents. Lithos,
1391 120, 30-41.
1392 Wells, P.R.A. (1977) Pyroxene thermometry in simple and complex systems. Contributions
1393 to Mineralogy and Petrology, 62, 129-139.
1394 Wiens, D.A., Kelley, K.A., & Plank, T. (2006) Mantle temperature variations beneath
1395 back-arc spreading centers inferred from seismology, petrology, and bathymetry.
1396 Earth and Planetary Science Letters, 248, 30-42.
1397 Yoshizawa, K., Miyake, K., and Yomogida, K. (2010) 3D upper mantle structure beneath
1398 Japan and its surrounding region from inter-station dispersion measurements of
1399 surface waves. Physics of the Earth and Planetary Interiors, 183, 4-19.
1400 Zhao, D., Hasegawa, A., and Horiuchi, S. (1992) Tomographic imaging of P and S wave
1401 velocity structure beneath northeastern Japan. Journal of Geophysical Research: Solid
1402 Earth, 97, 19909-19928.

Zheng, Y., Shen, W., Zhou, L., Yang, Y., Xie, Z., and Ritzwoller, M.H. (2011) Crust and uppermost mantle beneath the North China Craton, northeastern China, and the Sea of Japan from ambient noise tomography. Journal of Geophysical Research 116, 25, doi:10.1029/2011JB008637.

Figure captions

Fig. 1. Locations of Ichinomegata (a large open cross) and other volcanoes yielding mantle xenoliths in and around the Japan arc (small gray crosses) modified after Arai et al. (2007) and Harigane et al. (2011).

Fig. 2. Characteristic petrographic features of Ichinomegata xenoliths under an optical microscope (open nicol images: a, b, d, and h) and FE-SEM (back-scattered electron images: c, e, and f; a secondary electron image: g). Two contrasting textural types: (a) granular texture and (b) porphyroclastic texture. Microstructures commonly observed in granular samples are (c) symplectite consisting of clinopyroxene, orthopyroxene, and aluminous spinel; (d) amphibole and orthopyroxene partially rimming symplectite; and (e) “primary” plagioclase

(Prm-PL) and "secondary" plagioclase (2nd-PL). Glass indicating the presence of melt is commonly observed in porphyroclastic samples (f). Diamond-shaped aligned depression on the surface of olivine along grain boundaries (g) and fluid inclusions (arrows) in olivine (h), both suggesting the presence of fluid, are common in the granular samples. Abbreviations: OL = olivine, OPX = orthopyroxene, CPX = clinopyroxene, SPL = spinel, SYMP = two-pyroxene spinel symplectite after plagioclase, AMP = amphibole, PL = plagioclase, FLUID = fluid inclusion, and G = glass.

Fig. 3. Four types of chemical zoning (O1, O2, O3, and O4; Table 2) in large orthopyroxene grains recognized in Ca, Al, and Cr X-ray maps and a back-scattered electron image (BEI). Line profiles along solid lines in the BEIs are also shown. Abbreviations: apfu = atom per formula unit, Ca x5 = 5 times of Ca atom, Cr x10 = 10 times of Cr atom, and V = vesicles in glass. Other abbreviations are the same as in Figure 2. Sample names are given in the upper left corner of each panel. Chemical zoning of orthopyroxene in each xenolith is shown in Supplementary Figure S2.

1437

1438 **Fig. 4.** Three types of chemical zoning (C1, C2, and C3; Table 2) in large clinopyroxene
1439 grains recognized in Ca, Al, and Cr X-ray maps and BEI. Line profiles along solid
1440 lines in the BEIs are also shown. See Figures 2 and 3 for abbreviations. Sample
1441 names are given in the upper left corner of each panel. Chemical zoning of
1442 clinopyroxene in each xenolith is shown in Figure S2.

1443

1444 **Fig. 5.** Covariation of mean chemical compositions of olivine core and pyroxene rims
1445 (solid symbols) and cores (open symbols) with error bars (±1σ). Symbols for a
1446 pair of core and rim from the same sample are tied with gray thin lines. Black
1447 circles in Figures b, c, and f indicate Al_2O_3 contents, and the gray squares are ten
1448 times of Cr_2O_3 contents. The error for CaO contents of orthopyroxene rim is
1449 smaller than the size of symbols.

1450

1451 **Fig. 6.** Relationship between Mg# = Mg/(Mg+Fe) of olivine and Cr# = Cr/(Cr+Al) of
1452 spinel. Seven of the nine samples are plotted within the olivine-spinel upper
1453 mantle array (Arai, 1994), but two of them are too low in Mg# of olivine to be in

1454 the array field.

1455

1456 **Fig. 7.** Estimated pressures and temperatures of the examined xenoliths plotted with
1457 errors. In (a), two thin dashed lines for each sample represent isopleths giving a
1458 solution for the sample by applying a two-pyroxene geothermobarometer (T_{BKN};
1459 short-dashed line) and a Ca-in-orthopyroxene geothermobarometer ($T_{Ca\text{-}in\text{-}Opx}$;
1460 long-dashed line). In (b), a linearly regressed overall geotherm (a thick and gray
1461 line with dashed ends) and calculated error ellipses with a probability of 68 % are
1462 shown. The horizontal dot-dashed lines are seismic MOHO at 0.6 GPa (Iwasaki et
1463 al., 2013; Zhao et al., 1992) and the upper limit of seismic
1464 lithosphere-asthenosphere boundary at 1.8 GPa (Yoshizawa et al., 2010; Zheng et
1465 al., 2011).

1466

1467 **Fig. 8.** Reconstructed thermal, chemical, petrological, and rheological structures beneath
1468 Ichinomegata. The shallow levels (28-32 km) are characterized by low
1469 temperature, low oxygen fugacity, coarse granular texture, and the presence of
1470 amphibole, etched pits, and fluid inclusions (denoted as “fluid”), and the deep

levels (41-55 km) by high temperature, high oxygen fugacity, fine-grained porphyroclastic texture, and the presence of glass (denoted as "melt"). Sample numbers and estimated depth are shown in the far-left column. The dashed pattern in the bottom of columns for texture, Al phases, and melt/fluid imply a probable continuation of the features identified in the deeper samples. Abbreviations: LABZ = lithosphere-asthenosphere boundary zone, $\delta\log(fO_2)_{FMQ}$ = oxygen fugacity relative to the fayalite-magnetite-quartz buffer in log unit, Mg# = $Mg/(Mg+Fe^{2+})$, and Cr# = Cr/(Cr+Al). Other abbreviations are the same as in Figure 2.

Fig. 9. Comparison of the estimated pressures and temperatures with experimentally determined phase relations; (a) melting condition of hydrous peridotite (water-saturated and -undersaturated solidi of peridotite) and (b) the plagioclase-spinel phase transition and dry and wet solidi. Symbols in (a): filled circles = glass-bearing and amphibole-free peridotites, open circles = amphibole- and fluid-bearing lherzolites, and small triangles = other cases such as amphibole- and fluid-free lherzolite (HK64081206g) and amphibole-free but fluid-bearing lherzolite (IC81-5); in (b): filled squares = symplectite-free spinel lherzolites and

1488 open squares = symplectite-bearing plagioclase lherzolites. Line patterns are: thin
1489 solid lines = water-saturated solidi; thin dashed lines = water-undersaturated
1490 solidi; a thick dashed line = a dry solidus from Jaques and Green (1980); thick
1491 solid lines = spinel-plagioclase phase boundaries; and dotted lines = isopleths of
1492 Al in orthopyroxene in the plagioclase stability field (Gasparik, 2003). The shaded
1493 area in (b) indicates a possible pressure and temperature range for the formation of
1494 pyroxene-spinel symplectite from olivine and plagioclase. Its lower bound is
1495 defined by spinel-plagioclase phase transition (1) after Borghini et al. (2010) and
1496 the upper bound by the isopleth of Al in orthopyroxene (Gasparik, 2003) starting
1497 from the intersection of the dry solidus (Jaques and Green, 1980) and the
1498 spinel-plagioclase phase boundary of (1). The possible temperature-pressure
1499 region for the plagioclase lherzolites (shaded area) becomes narrower as shown by
1500 meshed pattern if wet solidus (Green, 1973) is used instead of the dry solidus.
1501
1502 **Fig. 10.** (a) Inferred depth variation of the lithosphere-asthenosphere boundary (LAB)
1503 along the E-W section of the Northeast Japan arc shown in Figure 1 from the
1504 back-arc basin (BAB) through back-arc (BA) to the Quaternary volcanic front

(QVF). A meshed area with its upper limit shown by a thick solid curve is LAB zone (10 km in thickness) inferred in our study. The inverted open triangle indicates the location of Ichinomegata. The dotted (A), dot-dashed (B), and dashed (C) vertical bars indicate locations and depth ranges of the thermal structure shown in (b). The depth is exaggerated, and the horizontal distance is measured from the Japan Trench. The depth of the MOHO is after Iwasaki et al., (2013). (b) Depth variations of temperature estimated from this study beneath Ichinomegata (B) and inferred for beneath the volcanic arc (A) and the back-arc basin (C). The locations and depth ranges of them are shown in (a). The thermal profiles of (A) and (C) are inferred by considering: (1) the upper limit of LAB zone corresponds to the wet solidus (Green, 1973), (2) the lithospheric thermal profile follows conductive geotherm, and (3) the thermal profile of LAB zone follows thermal gradient exhibited by the spinel peridotites beneath Ichinomegata. Open circles are estimated pressures and temperatures for the Ichinomegata xenoliths. The estimated condition for the magma generation of Sannomegata maar, one of the Megata maars occurring near Ichinomegata, is plotted as a white star in (a) and (b) and that of Iwate volcano, one of the volcanoes situated at the volcanic front and

to the east of Ichinomegata as a gray star (Kuritani et al., 2014a, 2014b). Note that the LAB becomes shallower and hotter with an increase in the geothermal gradient. A gray thick dot-dashed line in (b) is a linear extrapolation of the high pressure segment of the geotherm estimated from the Ichinomegata xenoliths, representing the thermal structure of LAB zone. The temperature of the melting condition for Sannomegata is higher than the Ichinomegata geotherm by ~100 °C at 60 km depth can be explained either (1) heat (and material) fluxed melting and (2) decompressional melting. See the main text for detail.

Table 1. Texture, grain size of olivine, modal composition of minerals, and microstructures

Sample	Rock type	Texture	Gr. size*[1] (mm)	Modal abundance (vol%)							Lamella in	
				Ol	Opx	Cpx	Spl	Pl	Amp	glass	Opx	Amp
HK64081206g	Pl lherzolite	granular	0.465	59	20	16	1	4	tr.*[2]		✓	✓
HK64081206c	Pl lherzolite	granular	0.466	58	28	7	1	tr.	6		✓	✓
HK64081206d	Spl lherzolite	weakly porphyroclastic	0.314	50	39	9	1		tr.	1*[4]	✓	✓
HK66031502	Pl lherzolite	granular	0.377	69	14	10	4	tr.	3		✓	✓
IC81-5	Spl lherzolite	porphyroclastic	0.291	73	20	6	1					
HK64081205a	Spl lherzolite	porphyroclastic	0.297	65	20	11	2		tr.*[3]	2	✓	
IC81-8	Spl lherzolite	porphyroclastic	0.205	65	23	11	1		tr.*[3]	tr.		
HK66031501	Spl lherzolite	porphyroclastic	0.259	65	22	9	2		tr.*[3]	2		
HK64081205b	Spl wehrlite	granular	0.527	81	2	15	1		tr.*[3]	1		

*[1] Sample mean diameters of olivine. *[2] Abundance of amphibole as lamellae in clinopyroxene. *[3] Abundance inclusions in clinopyroxene. *[4] Abundance of the fine-grained aggregates. Abbreviations: tr. = a trace amount (< symplectite, and pit & fl. inc. = the etch pits and the fluid inclusions on and in olivine.

in the samples.

Cpx		Lamella in Opx		Symp	pit & fl. inc.
Spl		Cpx	Spl		
✓		✓	✓	o	
✓		✓	✓	o	o
✓		✓	✓		o
✓		✓	✓	o	o
		✓			o
✓		✓	✓		
✓		✓	✓		
✓		✓	✓		
✓		✓			

: of amphibole as quench crystals and
≤0.5 vol. %), Symp = pyroxene-spinel

Table 2. Patterns of chemical zonings in orthopyroxene and clinopyroxene.

Zoning type	Samples	Elements	
		Ca	Al
Orthopyroxene			
O1	HK64081206g, HK64081206c	simple decrease	simple decrease
O2	HK64081206d	decrease followed by weak increase	decrease followed by wea
	HK66031502		decrease followed by weak increase
O3	HK64081205a, HK64081205b, HK66031501, IC81-8	decrease followed by intense increase	decrease followed by inter
O4	IC81-5	faint increase	faint decrease
Clinopyroxene			
C1	HK64081206g, HK64081206c, HK64081206d, HK66031502	simple increase	simple decrease
C2	HK64081205a, HK64081205b, HK66031501, IC81-8	simple decrease	simple increase decrease followed by inter
C3	IC81-5	flat	faint decrease followed by faint increase

Cr
ɛ
ık increase
simple decrease
ıse increase
ɛ
ɔr ıse increase
faint decrease

Sample	HK64081206g						
Mineral	Ol	Opx-c	Opx-r	Cpx-c	Cpx-r	Spl	Pl
Zoning		O1		C1			
N =	10	5	4	5	3	5	8
SiO_2	41.22	55.42	56.35	51.84	52.94	0.01	50.56
TiO_2	0.00	0.12	0.03	0.43	0.14	0.04	0.02
Al_2O_3	0.002	3.75	2.94	4.86	3.08	49.63	32.38
Cr_2O_3	0.00	0.50	0.30	1.17	0.47	18.98	0.01
FeO	9.13	6.05	5.80	2.42	2.19	11.89	0.11
MgO	50.45	32.99	34.26	15.53	16.72	19.32	0.06
CaO	0.031	0.68	0.43	22.81	23.15	0.00	15.20
MnO	0.13	0.15	0.15	0.07	0.07	0.15	0.02
NiO	0.39	0.08	0.09	0.05	0.05	0.30	0.01
Na_2O	0.00	0.06	0.03	0.68	0.43	0.00	2.83
K_2O	n.a.	0.02	n.a.	0.02	n.a.	n.a.	0.02
Total	101.36	99.82	100.35	99.87	99.23	100.01	101.21
Si	0.995	1.917	1.933	1.889	1.935	0.000	2.277
Ti	0.000	0.003	0.001	0.012	0.004	0.001	0.001
Al	0.000	0.153	0.119	0.209	0.133	1.558	1.718
Cr	0.000	0.014	0.008	0.034	0.014	0.400	0.000
Fe^{3+}	-	-	-	-	-	0.042	-
Fe^{2+}	0.184	0.175	0.166	0.074	0.067	0.223	0.004
Mg	1.815	1.701	1.752	0.843	0.911	0.767	0.004
Ca	0.001	0.025	0.016	0.891	0.906	0.000	0.734
Mn	0.003	0.004	0.004	0.002	0.002	0.003	0.001
Ni	0.008	0.002	0.003	0.002	0.001	0.006	0.000
Na	0.000	0.004	0.002	0.048	0.030	0.000	0.247
K	n.a.	0.001	n.a.	0.001	n.a.	n.a.	0.001
Total	3.005	3.999	4.003	4.003	4.003	3.000	4.987
Mg#	0.908	0.907	0.913	0.920	0.932	0.775	-
Cr#	-	0.082	0.063	0.139	0.093	0.204	-

Total Fe oxides as FeO. Cations are calculated based on 4 (olivin
Zoning types, O1, O2, O3, and O4 for orthopyroxene and C1, C2,
mean compositions of minerals are listed in Supplementary Table
Cr/(Cr+Al), n.a. = not analyzed, c = core, m = mantle, r = rim, ag

Table 3 (continued).

Sample	HK66031502									IC81-5				
Mineral	Ol	Opx-c	Opx-m	Opx-r	Cpx-c	Cpx-r	Spl	Pl	Amp	Ol	Opx-c	Opx-r	Cpx-c	Cpx-r
Zoning		O2			C1						O4		C3	
N =	8	4	1	5	5	5	5	5	5	11	5	4	3	4
SiO_2	40.73	55.60	56.09	56.11	52.03	53.33	0.00	49.99	43.52	40.66	56.43	55.45	53.76	52.67
TiO_2	0.00	0.12	0.03	0.05	0.39	0.18	0.11	0.03	0.27	0.00	0.04	0.04	0.09	0.09
Al_2O_3	0.002	3.82	3.17	3.19	4.27	2.88	46.33	31.32	15.44	0.011	3.58	3.61	3.55	3.61
Cr_2O_3	0.00	0.50	0.41	0.25	0.90	0.26	21.09	0.00	0.31	0.01	0.50	0.49	0.65	0.63
FeO	10.22	6.65	6.60	6.55	2.59	2.63	14.61	0.46	4.22	9.37	5.97	5.89	2.56	2.61
MgO	49.00	32.61	33.32	33.61	15.82	16.99	18.15	0.14	18.02	50.02	33.03	33.37	17.23	17.53
CaO	0.041	0.72	0.45	0.61	23.16	22.88	0.00	14.99	12.16	0.079	0.88	0.93	22.41	22.19
MnO	0.14	0.16	0.16	0.15	0.07	0.08	0.18	0.01	0.07	0.13	0.14	0.14	0.09	0.07
NiO	0.35	0.08	0.10	0.08	0.04	0.05	0.27	0.01	0.10	0.34	0.11	0.09	0.05	0.06
Na_2O	0.00	0.01	0.02	0.02	0.39	0.30	0.00	3.22	2.69	0.00	0.01	0.01	0.22	0.20
K_2O	n.a.	0.01	n.a.	n.a.	0.01	n.a.	n.a.	0.02	0.08	n.a.	0.00	n.a.	0.01	n.a.
Total	100.49	100.28	100.35	100.61	99.66	99.59	100.75	100.19	96.88	100.63	100.69	100.02	100.61	99.67
Si	0.997	1.918	1.932	1.927	1.900	1.942	0.000	2.283	6.205	0.990	1.932	1.915	1.933	1.915
Ti	0.000	0.003	0.001	0.001	0.011	0.005	0.002	0.001	0.029	0.000	0.001	0.001	0.002	0.003
Al	0.000	0.155	0.129	0.129	0.184	0.124	1.476	1.685	2.594	0.000	0.144	0.147	0.150	0.155
Cr	0.000	0.014	0.011	0.007	0.026	0.008	0.451	0.000	0.034	0.000	0.013	0.013	0.018	0.018
Fe^{3+}	-	-	-	-	-	-	0.071	-	-	-	-	-	-	-
Fe^{2+}	0.209	0.192	0.190	0.188	0.079	0.080	0.259	0.017	0.503	0.191	0.171	0.170	0.077	0.079
Mg	1.787	1.677	1.711	1.721	0.861	0.922	0.731	0.009	3.830	1.816	1.686	1.717	0.924	0.950
Ca	0.001	0.027	0.016	0.022	0.906	0.893	0.000	0.733	1.857	0.002	0.032	0.034	0.863	0.864
Mn	0.003	0.005	0.005	0.004	0.002	0.002	0.004	0.000	0.009	0.003	0.004	0.004	0.003	0.002
Ni	0.007	0.002	0.003	0.002	0.001	0.001	0.006	0.000	0.012	0.007	0.003	0.003	0.001	0.002
Na	0.000	0.001	0.001	0.001	0.028	0.021	0.000	0.285	0.742	0.000	0.001	0.001	0.015	0.014
K	0.000	0.000	n.a.	n.a.	0.000	n.a.	n.a.	0.001	0.014	n.a.	0.000	0.000	0.000	0.000
Total	3.003	3.995	3.998	4.004	3.998	3.998	3.000	5.016	15.830	3.009	3.988	4.005	3.988	4.003
Mg#	0.895	0.897	0.900	0.901	0.916	0.920	0.739	-	0.884	0.905	0.908	0.910	0.923	0.923
Cr#	-	0.080	0.080	0.050	0.124	0.058	0.234	-	0.013	-	0.085	0.083	0.110	0.105

	HK64081205a								
Spl	Ol	Opx-c	Opx-m	Opx-r	Cpx-c	Cpx-r	Spl	Amp	glass
		O3			C2				
5	11	3	1	5	4	5	5	1	10
0.03	40.72	55.25	55.80	54.61	52.39	51.99	0.03	42.35	54.24
0.07	0.00	0.11	0.08	0.14	0.19	0.43	0.18	1.60	0.79
47.18	0.015	3.64	3.58	4.77	3.97	5.71	49.54	15.12	20.05
21.49	0.01	0.48	0.29	0.38	0.51	0.55	16.14	0.97	0.04
11.52	10.21	6.53	6.43	6.90	3.24	3.44	14.06	4.40	3.76
18.92	49.14	33.27	33.29	31.95	16.90	16.50	19.20	17.69	2.73
0.00	0.090	0.72	0.49	1.02	22.44	21.62	0.00	11.60	9.67
0.16	0.17	0.14	0.13	0.16	0.09	0.10	0.16	0.06	0.10
0.29	0.36	0.08	0.08	0.10	0.06	0.05	0.34	0.11	0.01
0.00	0.00	0.02	0.01	0.03	0.31	0.37	0.00	2.24	2.58
n.a.	n.a.	0.00	n.a.	n.a.	0.00	n.a.	n.a.	1.03	1.21
99.66	100.72	100.23	100.17	100.06	100.10	100.75	99.66	97.17	95.17
0.001	0.994	1.909	1.923	1.893	1.905	1.874	0.001	6.071	-
0.001	0.000	0.003	0.002	0.004	0.005	0.012	0.004	0.172	-
1.504	0.000	0.148	0.146	0.195	0.170	0.242	1.563	2.555	-
0.460	0.000	0.013	0.008	0.010	0.015	0.016	0.341	0.109	-
0.034	-	-	-	-	-	-	0.091	-	-
0.227	0.209	0.189	0.185	0.200	0.098	0.104	0.223	0.528	-
0.763	1.789	1.713	1.710	1.651	0.915	0.887	0.766	3.781	-
0.000	0.002	0.026	0.018	0.038	0.874	0.835	0.000	1.781	-
0.004	0.003	0.004	0.004	0.005	0.003	0.003	0.004	0.008	-
0.006	0.007	0.002	0.002	0.003	0.002	0.001	0.007	0.013	-
0.000	0.000	0.001	0.001	0.002	0.022	0.026	0.000	0.623	-
n.a.	n.a.	0.000	n.a.	n.a.	0.000	0.000	n.a.	0.189	-
3.000	3.005	4.008	3.999	4.001	4.009	3.999	3.000	15.830	-
0.771	0.896	0.901	0.902	0.892	0.903	0.895	0.774	0.878	0.564
0.234	-	0.081	0.051	0.050	0.079	0.061	0.179	0.041	0.001

Table 3 (continued).

Sample	IC81-8									HK660315(				
Mineral	Ol	Opx-c	Opx-m	Opx-r	Cpx-c	Cpx-m	Cpx-r	Spl	glass	Ol	Opx-c	Opx-m	Opx-r	Cpx-c
Zoning		O3			C2						O3			
N =	11	5	1	5	4	1	5	5	1	11	5	1	5	5
SiO_2	40.40	55.58	55.99	55.28	52.64	52.92	51.87	0.03	57.75	40.63	55.36	54.96	54.83	52.44
TiO_2	0.00	0.09	0.07	0.08	0.24	0.18	0.31	0.15	0.73	0.00	0.07	0.05	0.13	0.18
Al_2O_3	0.016	3.67	3.68	3.60	3.80	3.33	5.11	48.28	21.28	0.016	3.76	3.83	4.82	4.42
Cr_2O_3	0.01	0.50	0.51	0.33	0.49	0.31	0.66	17.40	0.01	0.01	0.51	0.49	0.35	0.54
FeO	10.26	6.82	6.64	6.66	3.21	3.08	3.43	15.07	2.86	9.73	6.51	6.43	6.29	3.24
MgO	49.43	32.54	33.26	32.89	16.90	17.43	16.78	18.75	1.97	49.23	32.69	32.83	32.45	16.58
CaO	0.088	0.69	0.54	1.00	22.35	22.19	21.53	0.00	7.14	0.090	0.72	0.51	1.01	22.35
MnO	0.16	0.16	0.14	0.16	0.08	0.04	0.11	0.16	0.05	0.16	0.15	0.17	0.16	0.09
NiO	0.34	0.09	0.09	0.09	0.05	0.07	0.05	0.32	0.00	0.37	0.09	0.08	0.09	0.06
Na_2O	0.00	0.02	0.00	0.02	0.33	0.33	0.42	0.00	3.20	0.00	0.02	0.02	0.02	0.32
K_2O	n.a.	0.00	n.a.	n.a.	0.00	n.a.	n.a.	n.a.	1.60	n.a.	0.00	n.a.	n.a.	0.00
Total	100.70	100.17	100.93	100.10	100.10	99.87	100.27	100.17	96.58	100.24	99.89	99.35	100.15	100.22
Si	0.988	1.921	1.919	1.914	1.912	1.923	1.880	0.001	-	0.995	1.917	1.913	1.893	1.902
Ti	0.000	0.002	0.002	0.002	0.007	0.005	0.008	0.003	-	0.000	0.002	0.001	0.003	0.005
Al	0.000	0.150	0.149	0.147	0.163	0.142	0.218	1.527	-	0.000	0.153	0.157	0.196	0.189
Cr	0.000	0.014	0.014	0.009	0.014	0.009	0.019	0.369	-	0.000	0.014	0.013	0.009	0.016
Fe^{3+}	-	-	-	-	-	-	-	0.099	-	-	-	-	-	-
Fe^{2+}	0.210	0.197	0.190	0.193	0.098	0.093	0.104	0.239	-	0.199	0.188	0.187	0.182	0.098
Mg	1.802	1.677	1.699	1.697	0.915	0.944	0.907	0.750	-	1.797	1.688	1.703	1.671	0.896
Ca	0.002	0.025	0.020	0.037	0.870	0.864	0.836	0.000	-	0.002	0.027	0.019	0.037	0.869
Mn	0.003	0.005	0.004	0.005	0.002	0.001	0.003	0.004	-	0.003	0.004	0.005	0.005	0.003
Ni	0.007	0.003	0.003	0.002	0.002	0.002	0.002	0.007	-	0.007	0.002	0.002	0.003	0.002
Na	0.000	0.002	0.000	0.001	0.024	0.023	0.029	0.000	-	0.000	0.002	0.001	0.001	0.023
K	n.a.	0.000	n.a.	n.a.	0.000	n.a.	n.a.	n.a.	-	0.000	0.000	n.a.	n.a.	0.000
Total	3.012	3.995	3.998	4.007	4.005	4.008	4.007	3.000	-	3.005	3.998	4.002	4.001	4.002
Mg#	0.896	0.895	0.899	0.898	0.904	0.910	0.897	0.758	0.550	0.900	0.899	0.901	0.902	0.901
Cr#	-	0.084	0.084	0.058	0.080	0.059	0.080	0.195	0.000	-	0.084	0.078	0.046	0.076

01				HK64081205b							
Cpx-m	Cpx-r	Spl	glass	Ol	Opx-c	Opx-m	Opx-r	Cpx-c	Cpx-r	Spl	glass
C2						O3			C2		
1	5	5	12	11	3	1	4	3	3	5	20
52.58	50.94	0.02	56.70	39.99	55.16	55.51	54.16	52.59	51.42	0.05	48.90
0.12	0.44	0.15	0.69	0.00	0.12	0.09	0.14	0.57	0.38	0.26	2.00
3.95	5.85	47.34	20.46	0.012	3.50	3.41	4.44	4.90	5.51	48.43	21.52
0.32	0.62	19.06	0.01	0.01	0.43	0.39	0.41	1.01	0.66	14.62	0.01
3.10	3.37	14.26	3.17	12.61	6.75	6.97	7.87	2.99	4.24	19.17	6.71
17.06	16.37	19.16	2.04	47.20	32.69	33.13	31.76	15.87	16.24	17.53	3.02
22.06	21.42	0.00	8.25	0.087	0.60	0.49	1.08	22.09	20.88	0.00	10.48
0.10	0.10	0.17	0.09	0.19	0.16	0.17	0.17	0.09	0.12	0.17	0.13
0.09	0.05	0.34	0.01	0.28	0.07	0.10	0.08	0.03	0.04	0.27	0.02
0.32	0.37	0.00	2.82	0.00	0.03	0.02	0.03	0.48	0.39	0.00	3.69
n.a.	n.a.	n.a.	1.43	n.a.	n.a.	n.a.	n.a.	n.a.	n.a.	n.a.	1.80
99.70	99.53	100.50	95.67	100.38	99.52	100.27	100.14	100.60	99.89	100.50	98.29
1.914	1.861	0.001	-	0.991	1.919	1.918	1.887	1.898	1.875	0.001	-
0.003	0.012	0.003	-	0.000	0.003	0.002	0.004	0.016	0.011	0.005	-
0.169	0.252	1.496	-	0.000	0.144	0.139	0.182	0.208	0.237	1.537	-
0.009	0.018	0.404	-	0.000	0.012	0.011	0.011	0.029	0.019	0.311	-
-	-	0.096	-	-	-	-	-	-	-	0.145	-
0.094	0.103	0.223	-	0.261	0.196	0.202	0.229	0.090	0.129	0.287	-
0.926	0.891	0.766	-	1.744	1.696	1.707	1.650	0.853	0.883	0.704	-
0.860	0.838	0.000	-	0.002	0.023	0.018	0.040	0.854	0.815	0.000	-
0.003	0.003	0.004	-	0.004	0.005	0.005	0.005	0.003	0.004	0.004	-
0.003	0.001	0.007	-	0.006	0.002	0.003	0.002	0.001	0.001	0.006	-
0.023	0.026	0.000	-	0.000	0.002	0.001	0.002	0.033	0.028	0.000	-
n.a.	n.a.	n.a.	-	n.a.	n.a.	n.a.	n.a.	n.a.	n.a.	n.a.	-
4.005	4.006	3.000	-	3.009	4.001	4.005	4.013	3.985	4.001	3.000	-
0.908	0.897	0.774	0.534	0.870	0.896	0.894	0.878	0.905	0.872	0.710	0.445
0.052	0.067	0.213	0.000	-	0.076	0.071	0.058	0.121	0.075	0.168	0.000

Table 4. Mean chemical compositions at the rim of pyroxenes with analytical errors, and estimated pressures

Sample	HK64081206g				HK64081206c				HK64081206d				I
Minerals	Opx-r	1 σ	Cpx-r	1 σ	Opx-r	1 σ	Cpx-r	1 σ	Opx-r	1 σ	Cpx-r	1 σ	Opx-r
N =	4		3		4		5		4		4		5
SiO_2	56.35	.284	52.94	.174	56.43	.208	52.70	.209	57.17	.121	53.97	.084	56.11
TiO_2	0.03	.007	0.14	.022	0.03	.002	0.30	.038	0.06	.013	0.08	.008	0.05
Al_2O_3	2.94	.280	3.08	.234	2.52	.175	3.79	.181	1.22	.057	1.23	.036	3.19
Cr_2O_3	0.30	.134	0.47	.062	0.14	.071	0.80	.079	0.23	.025	0.31	.026	0.25
FeO	5.80	.067	2.19	.033	6.25	.035	2.42	.106	7.34	.226	2.81	.102	6.55
MgO	34.26	.327	16.72	.141	34.15	.214	16.38	.192	33.94	.403	17.64	.284	33.61
CaO	0.43	.002	23.15	.016	0.41	.003	23.44	.080	0.52	.009	23.58	.077	0.61
MnO	0.15	.007	0.07	.001	0.14	.006	0.07	.007	0.20	.018	0.09	.008	0.15
NiO	0.09	.003	0.05	.009	0.09	.002	0.04	.008	0.07	.006	0.03	.006	0.08
Na_2O	0.03	.029	0.43	.014	0.00	.005	0.36	.027	0.01	.004	0.20	.018	0.02
Total	100.35		99.23		100.16		100.28		100.75		99.95		100.61
P (GPa)	0.72 ± 0.52				0.80 ± 0.70				-0.50 (0.82) ± 0.61				
T (°C)	829 ± 23				828 ± 30				811 (875) ± 27				

Total Fe oxides as FeO. "N" is a number of data used for calculation of a average chemical composition. "σ" estimates are shown with one standard deviation values. The pressure and the temperature of HK640812(geotherm and $T_{Ca\text{-}in\text{-}Opx}$.

Table 4 (continued)**.**

Sample	HK64081205a				IC81-8				HK66031501				H
Minerals	Opx-r	1 σ	Cpx-r	1 σ	Opx-r	1 σ	Cpx-r	1 σ	Opx-r	1 σ	Cpx-r	1 σ	Opx-r
Ave. no.	5		5		5		5		5		5		4
SiO_2	54.61	.489	51.99	.227	55.28	.276	51.87	.186	54.83	.392	50.94	.205	54.16
TiO_2	0.14	.023	0.43	.045	0.08	.011	0.31	.018	0.13	.015	0.44	.047	0.14
Al_2O_3	4.77	.239	5.71	.111	3.60	.323	5.11	.116	4.82	.187	5.85	.177	4.44
Cr_2O_3	0.38	.028	0.55	.049	0.33	.074	0.66	.029	0.35	.042	0.62	.171	0.41
FeO	6.90	.115	3.44	.119	6.66	.170	3.43	.066	6.29	.147	3.37	.083	7.87
MgO	31.95	.157	16.50	.080	32.89	.185	16.78	.160	32.45	.108	16.37	.122	31.76
CaO	1.02	.008	21.62	.075	1.00	.003	21.53	.135	1.01	.005	21.42	.123	1.08
MnO	0.16	.022	0.10	.008	0.16	.007	0.11	.029	0.16	.007	0.10	.014	0.17
NiO	0.10	.020	0.05	.004	0.09	.004	0.05	.017	0.09	.003	0.05	.010	0.08
Na_2O	0.03	.007	0.37	.026	0.02	.006	0.42	.048	0.02	.003	0.37	.044	0.03
Total	100.06		100.75		100.10		100.27		100.15		99.53		100.14
P (GPa)	1.29 ± 0.24				1.46 ± 0.37				1.51 ± 0.36				

T (°C)	1050 ± 12	1052 ± 19	1057 ± 18

s and temperatures of the Ichinomegata xenoliths.

HK66031502			IC81-5			
1 σ	Cpx-r 5	1 σ	Opx-r 4	1 σ	Cpx-r 4	1 σ
.202	53.33	.177	55.45	.132	52.67	.241
.014	0.18	.018	0.04	.005	0.09	.009
.258	2.88	.200	3.61	.011	3.61	.013
.118	0.26	.019	0.49	.005	0.63	.011
.168	2.63	.088	5.89	.032	2.61	.049
.408	16.99	.156	33.37	.185	17.53	.230
.005	22.88	.061	0.93	.002	22.19	.053
.014	0.08	.009	0.14	.008	0.07	.045
.002	0.05	.004	0.09	.005	0.06	.030
.015	0.30	.010	0.01	.005	0.20	.029
	99.59		100.02		99.67	
0.85 ± 0.42			1.16 ± 0.29			
905 ± 19			1017 ± 15			

' is a standard deviation. Pressure and temperature
06d in brackets are based on the sample-derived

HK64081205b		
1 σ	Cpx-r 3	1 σ
.252	51.42	.250
.003	0.38	.048
.145	5.51	.297
.044	0.66	.111
.124	4.24	.100
.181	16.24	.456
.006	20.88	.127
.007	0.12	.010
.009	0.04	.005
.002	0.39	.029
	99.89	
1.62 ± 0.44		

1081 ± 23

Table 5. Summary of depth variations of all the features observed or estimated for the Ichi

Sample	Pressure (GPa)	Depth (km)	Temperature (°C)	Olivine compositions		
				Ca (ppm)	NiO (wt.%)	MnO (
HK64081206g	0.72 ± .52	28 ± 16	829 ± 23	219 ± 10	0.390 ± .007	0.128
HK64081206c	0.80 ± .70	30 ± 21	828 ± 30	216 ± 10	0.396 ± .003	0.140
HK64081206d	(0.82)	(31)	(875)	287 ± 70	0.280 ± .012	0.168
HK66031502	0.85 ± .42	32 ± 13	905 ± 19	294 ± 10	0.349 ± .005	0.145
IC81-5	1.16 ± .29	41 ± 9	1017 ± 15	566 ± 16	0.342 ± .016	0.134
HK64081205a	1.29 ± .24	45 ± 7	1050 ± 12	645 ± 19	0.365 ± .006	0.167
IC81-8	1.46 ± .37	50 ± 11	1052 ± 19	627 ± 14	0.339 ± .004	0.156
HK66031501	1.51 ± .36	52 ± 11	1057 ± 18	643 ± 18	0.367 ± .003	0.161
HK64081205b	1.62 ± .44	55 ± 13	1081 ± 23	624 ± 31	0.283 ± .022	0.191

The pressure, depth, and temperature of HK64081206d in brackets are based on the sample-derived geo

nomegata xenoliths.

wt.%)	Mg#	$\delta\log(fO_2)_{FMQ}$
± .006	0.908	-0.49
± .005	0.902	+0.19
± .027	0.881	+1.94
± .003	0.895	+0.08
± .005	0.905	-1.27
± .006	0.896	+0.31
± .005	0.896	+0.39
± .003	0.900	+0.32
± .007	0.870	+0.69

therm and $T_{Ca\text{-}in\text{-}Opx}$ (Table 4).

Table 5. (continued)

Sample	Al-rich phase	Hydrous phases	Texture	Gr. Size (mm)
HK64081206g	Pl	n.d.	granular	0.465
HK64081206c	Pl	Amp + fluid	granular	0.466
HK64081206d	Spl	Amp + fluid + Agg.	weakly porphyroclastic	0.314
HK66031502	Pl	Amp + fluid	granular	0.377
IC81-5	Spl	fluid	porphyroclastic	0.291
HK64081205a	Spl	melt	porphyroclastic	0.297
IC81-8	Spl	melt	porphyroclastic	0.205
HK66031501	Spl	melt	porphyroclastic	0.259
HK64081205b	Spl	melt	granular	0.527

Agg. = fine-grained crystal aggregate after melt; n.d. = not detected. The occurr
clinopyroxene and quench crystals in glass are excluded.

Chemical zoning of pyroxenes	
Types	Decoded thermal history
O1 & C1	Simple cooling.
O1 & C1	Simple cooling.
O2 & C1	Cooling followed by weak heating.
O2 & C1	Cooling followed by weak heating.
O4 & C3	Cooling and long heating.
O3 & C2	Cooling followed by intense heating.
O3 & C2	Cooling followed by intense heating.
O3 & C2	Cooling followed by intense heating.
O3 & C2	Cooling followed by intense heating.

ences of amphibole as lamellae and inclusions in

Figure 1.

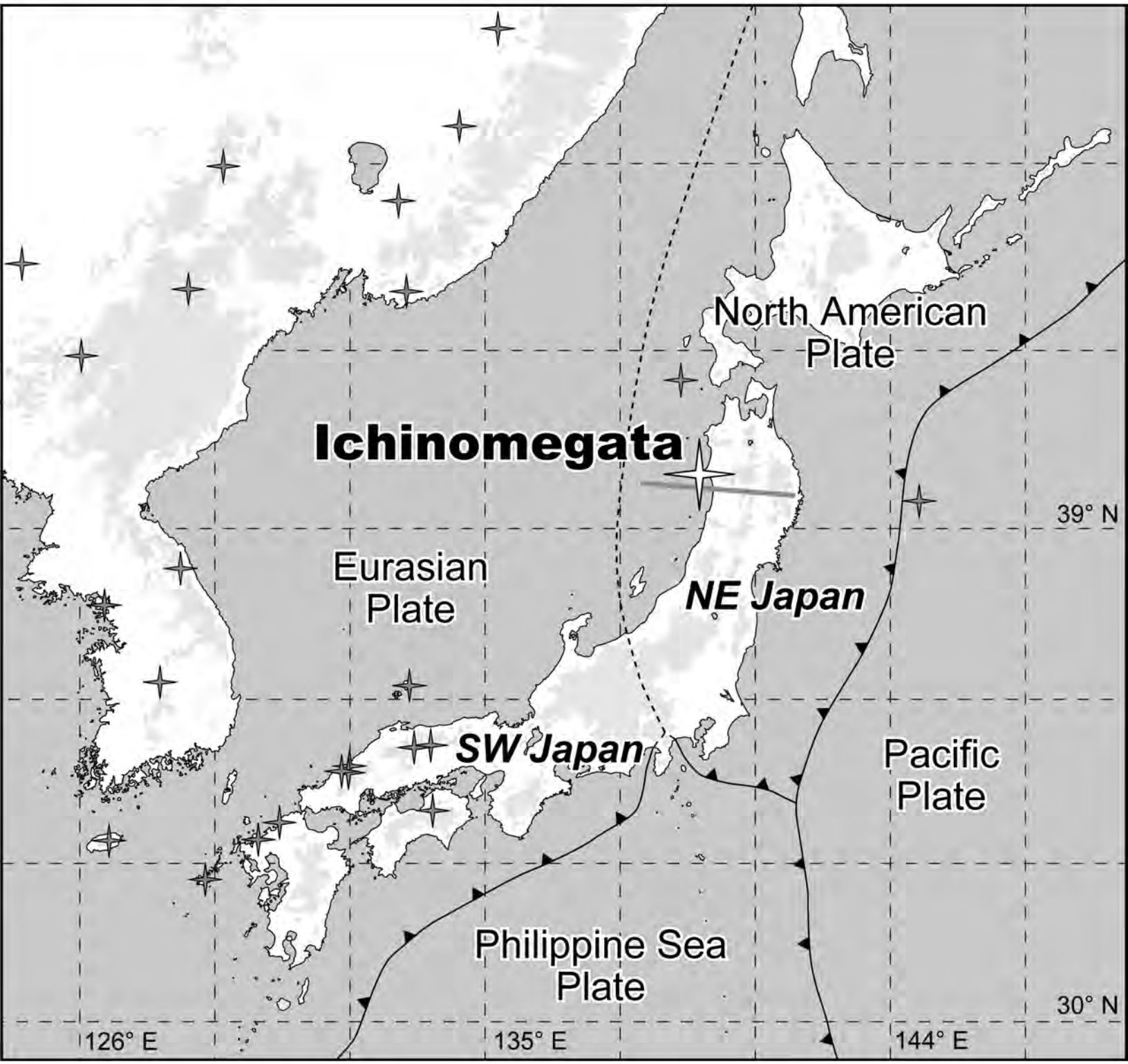
North American Plate
Ichinomegata
39° N
Eurasian Plate
NE Japan
SW Japan
Pacific Plate
Philippine Sea Plate
30° N
126° E
135° E
144° E

Figure 2.

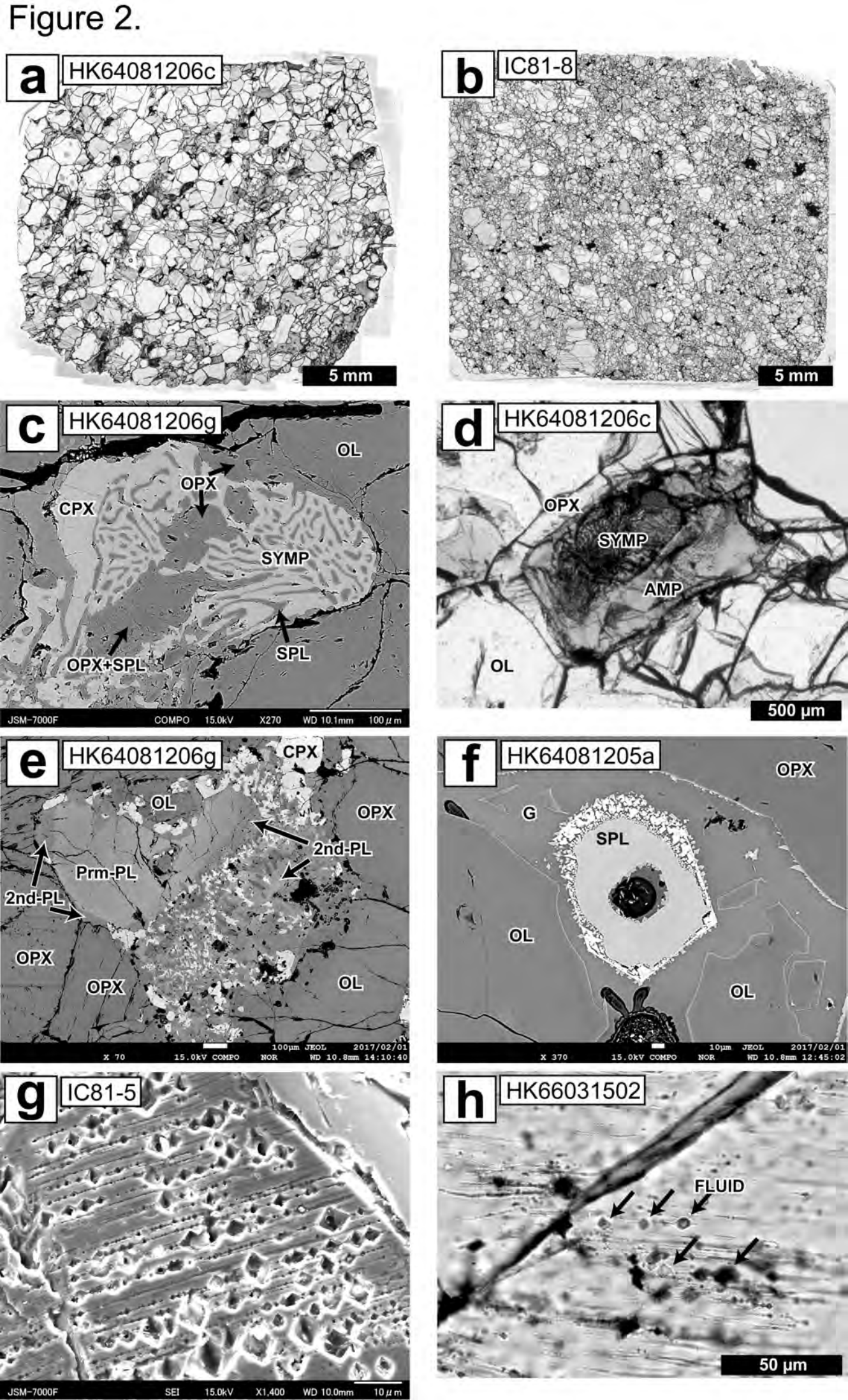
a
HK64081206c
5 mm
b
IC81-8
5 mm
c
HK64081206g
OL
OPX
CPX
SYMP
SPL
OPX+SPL
JSM-7000F COMPO 15.0kV X270 WD 10.1mm 100 μm
d
HK64081206c
OPX
SYMP
AMP
OL
500 μm
e
HK64081206g
CPX
OL
OPX
2nd-PL
Prm-PL
2nd-PL
OPX
OPX
OL
X 70 15.0kV COMPO NOR WD 10.8mm 14:10:40 100μm JEOL 2017/02/01
f
HK64081205a
OPX
G
SPL
OL
OL
X 370 15.0kV COMPO NOR WD 10.8mm 12:45:02 10μm JEOL 2017/02/01
g
IC81-5
JSM-7000F SEI 15.0kV X1,400 WD 10.0mm 10 μm
h
HK66031502
FLUID
50 μm

Figure 3.

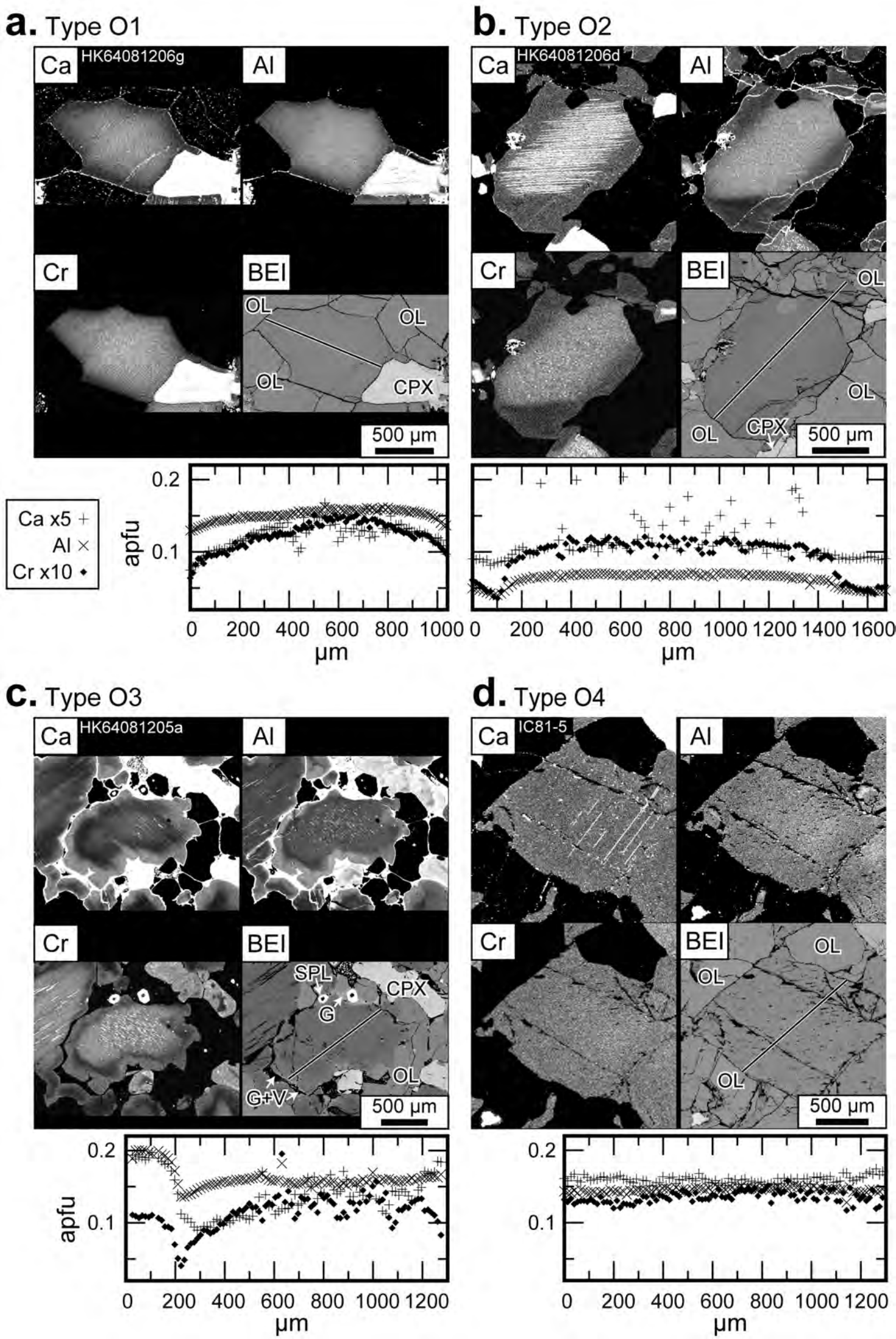
a. Type O1
HK64081206g
Ca
Al
Cr
BEI
OL
OL
OL
CPX
500 µm
b. Type O2
HK64081206d
Ca
Al
Cr
BEI
OL
OL
OL
CPX
500 µm
Ca x5
Al
Cr x10
apfu
0.2
0.1
0 200 400 600 800 1000
µm
0 200 400 600 800 1000 1200 1400 1600
µm
c. Type O3
HK64081205a
Ca
Al
Cr
BEI
SPL
CPX
G
OL
G+V
500 µm
d. Type O4
IC81-5
Ca
Al
Cr
BEI
OL
OL
OL
500 µm
apfu
0.2
0.1
0 200 400 600 800 1000 1200
µm
0 200 400 600 800 1000 1200
µm

Figure 4.

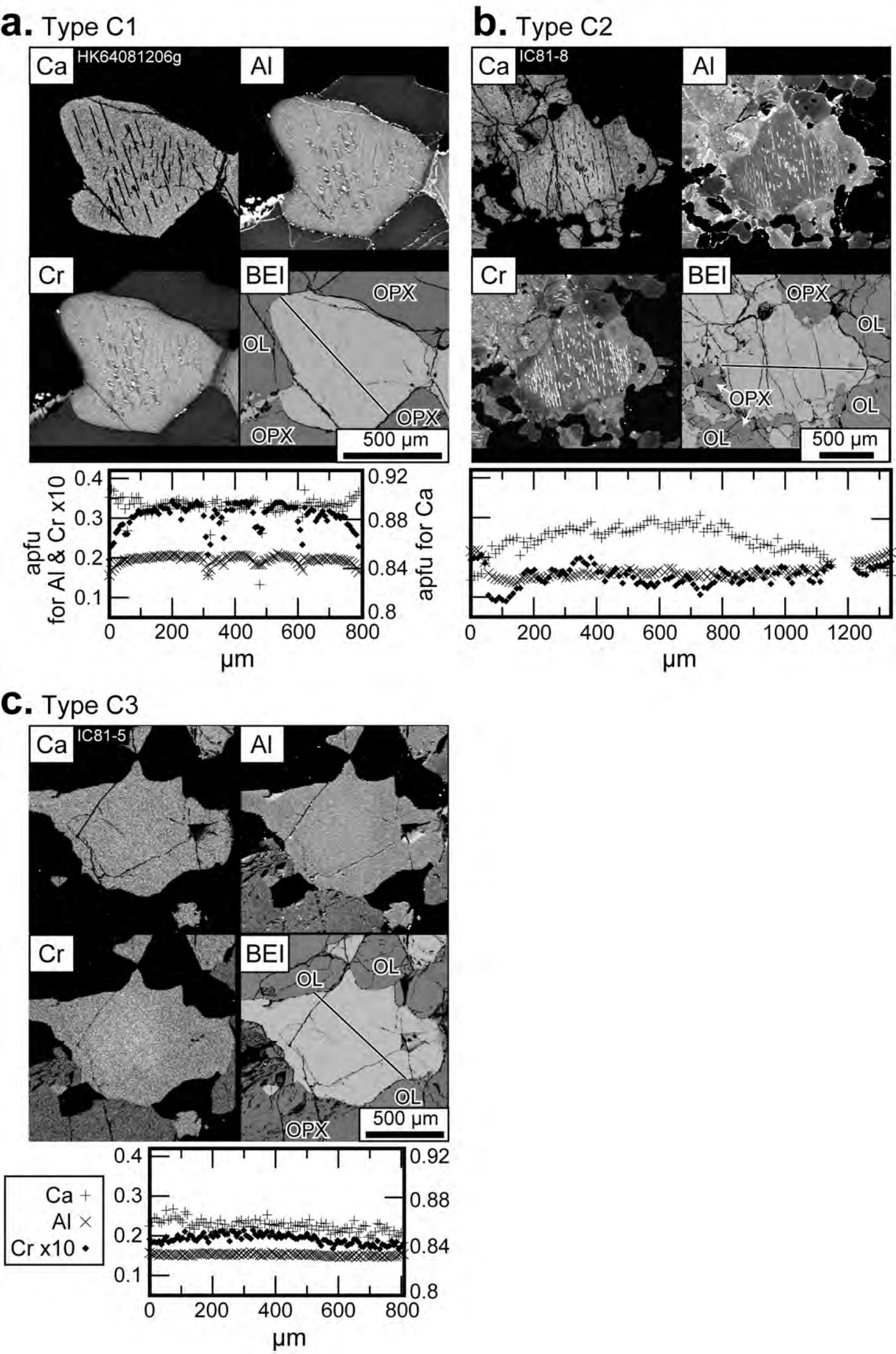
a. Type C1
Ca
HK64081206g
Al
Cr
BEI
OPX
OL
OPX
OPX
500 µm
apfu for Al & Cr x10
apfu for Ca
0.4
0.3
0.2
0.1
0.92
0.88
0.84
0.8
0
200
400
600
800
µm
b. Type C2
Ca
IC81-8
Al
Cr
BEI
OPX
OL
OPX
OL
OL
500 µm
0
200
400
600
800
1000
1200
µm
c. Type C3
Ca
IC81-5
Al
Cr
BEI
OL
OL
OL
OPX
500 µm
Ca +
Al ×
Cr x10 •
0.4
0.3
0.2
0.1
0.92
0.88
0.84
0.8
0
200
400
600
800
µm

Figure 5.

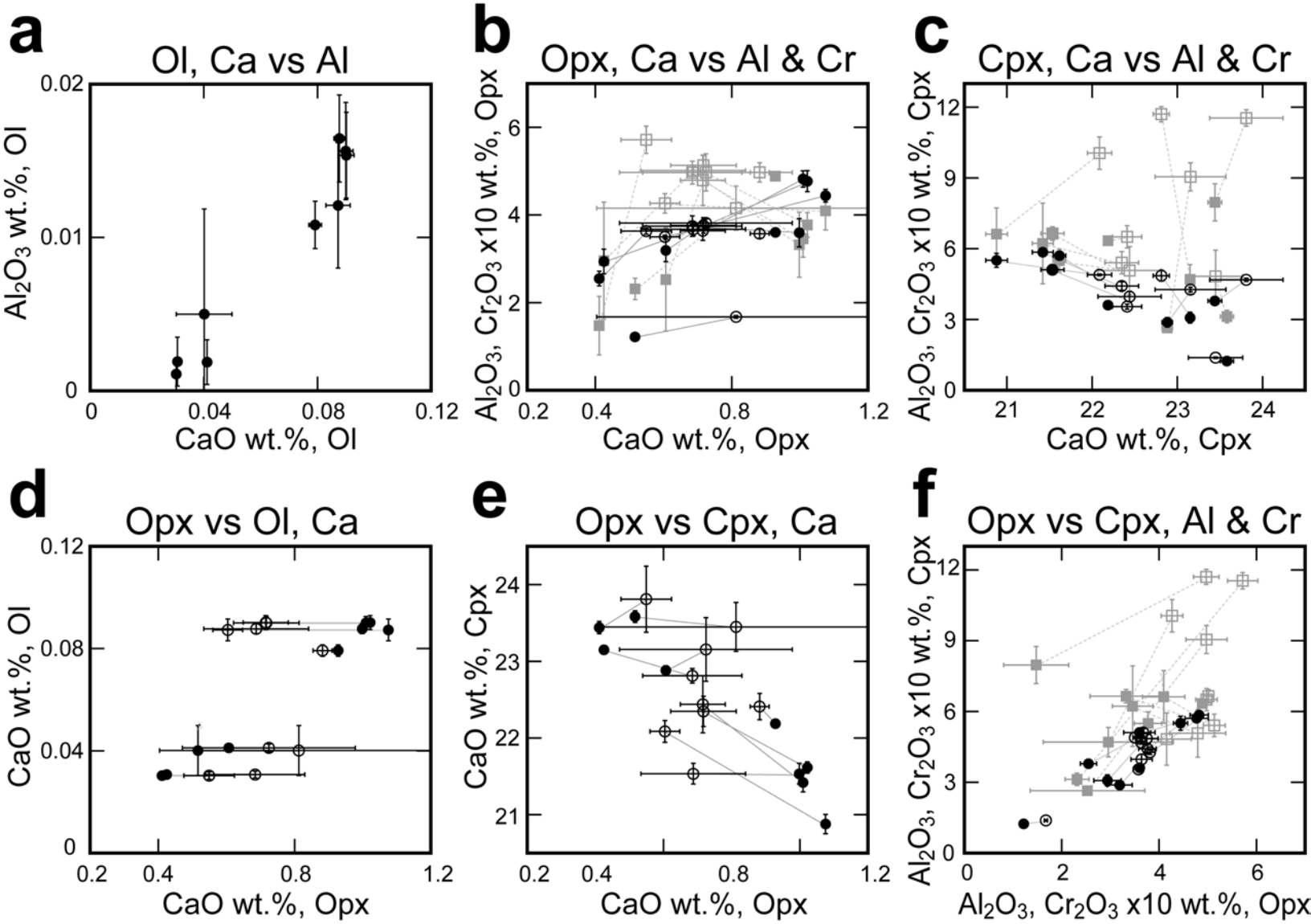
a
Ol, Ca vs Al
Al_2O_3 wt.%, Ol
CaO wt.%, Ol
b
Opx, Ca vs Al & Cr
Al_2O_3, Cr_2O_3 x10 wt.%, Opx
CaO wt.%, Opx
c
Cpx, Ca vs Al & Cr
Al_2O_3, Cr_2O_3 x10 wt.%, Cpx
CaO wt.%, Cpx
d
Opx vs Ol, Ca
CaO wt.%, Ol
CaO wt.%, Opx
e
Opx vs Cpx, Ca
CaO wt.%, Cpx
CaO wt.%, Opx
f
Opx vs Cpx, Al & Cr
Al_2O_3, Cr_2O_3 x10 wt.%, Cpx
Al_2O_3, Cr_2O_3 x10 wt.%, Opx

Figure 6.

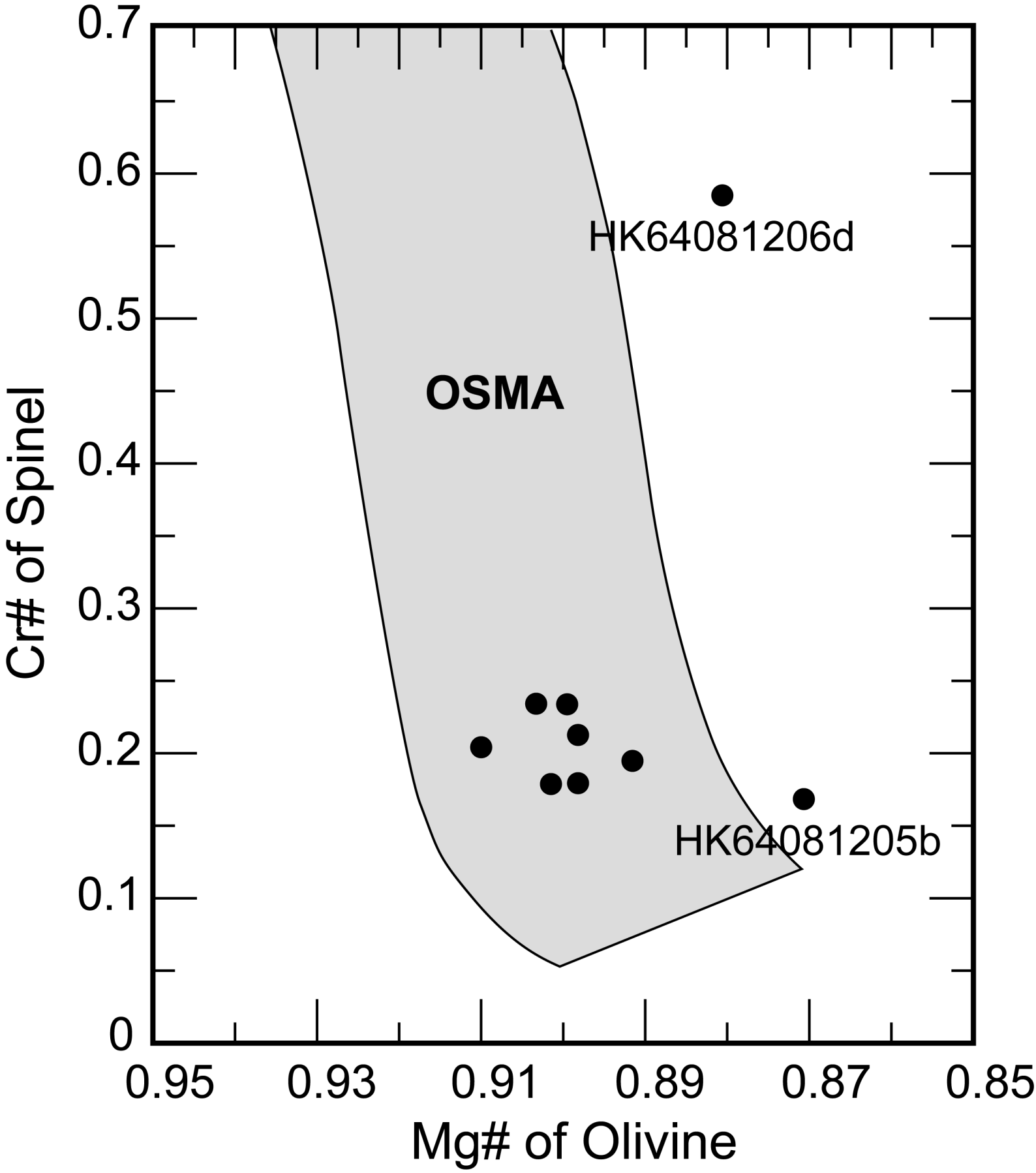
0.7
0.6
0.5
0.4
0.3
0.2
0.1
0
Cr# of Spinel
HK64081206d
OSMA
HK64081205b
0.95
0.93
0.91
0.89
0.87
0.85
Mg# of Olivine

Figure 7.

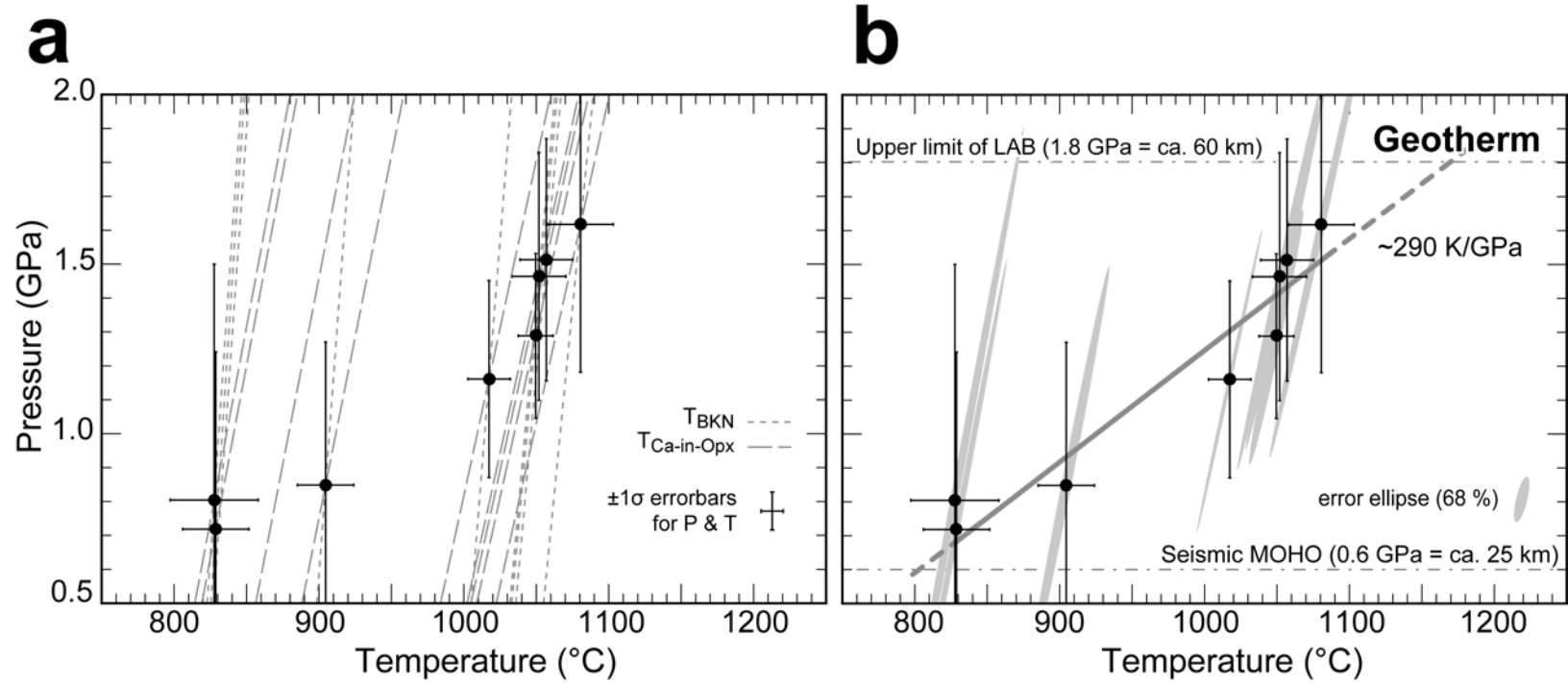
a
b
2.0
1.5
1.0
0.5
Pressure (GPa)
800
900
1000
1100
1200
Temperature (°C)
T_BKN
T_Ca-in-Opx
±1σ errorbars for P & T
Upper limit of LAB (1.8 GPa = ca. 60 km)
Geotherm
~290 K/GPa
error ellipse (68 %)
Seismic MOHO (0.6 GPa = ca. 25 km)

Figure 8.

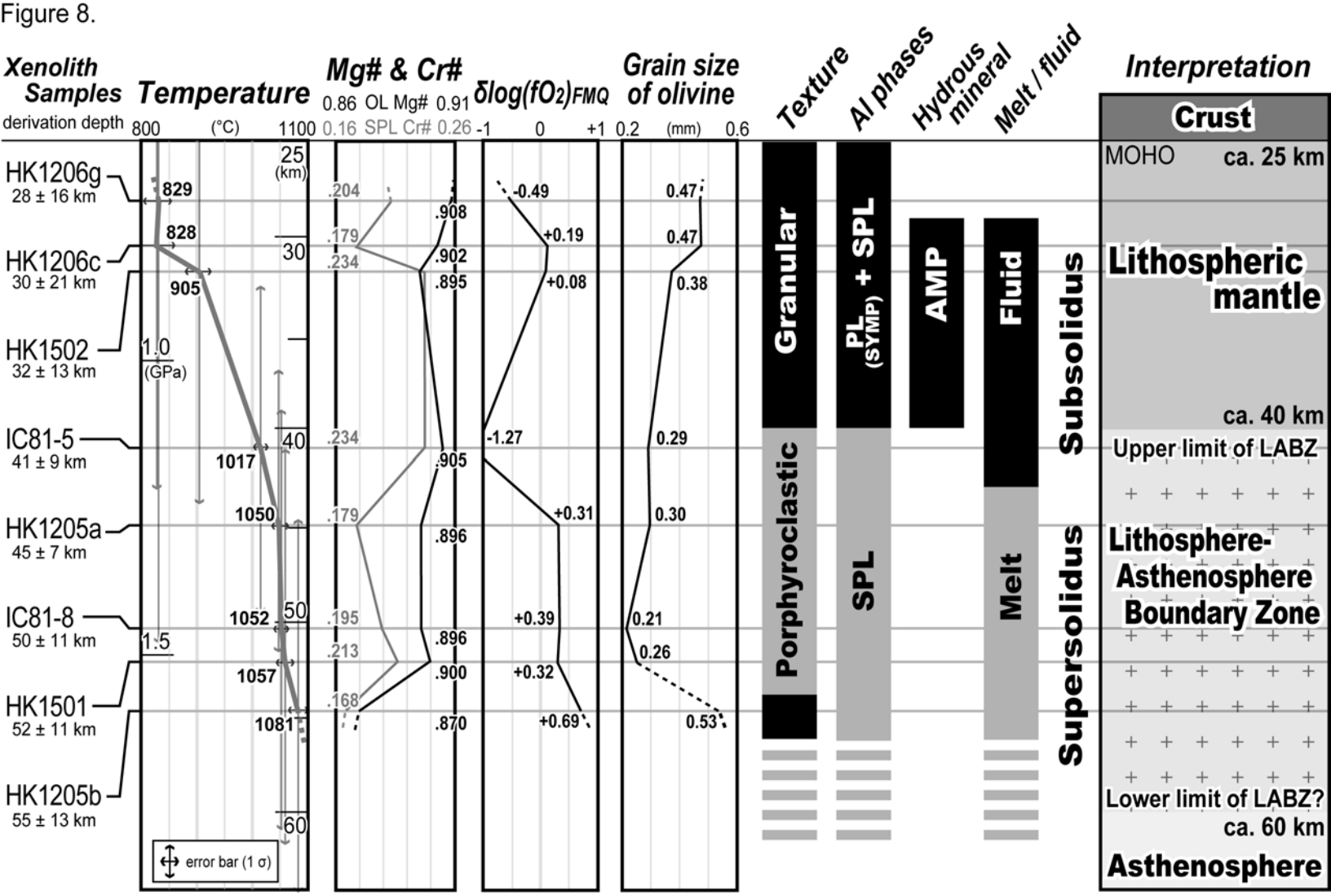
Xenolith Samples
derivation depth
Temperature
800
(°C)
1100
25
(km)
30
40
50
60
1.0
(GPa)
1:5
HK1206g
28 ± 16 km
HK1206c
30 ± 21 km
HK1502
32 ± 13 km
IC81-5
41 ± 9 km
HK1205a
45 ± 7 km
IC81-8
50 ± 11 km
HK1501
52 ± 11 km
HK1205b
55 ± 13 km
829
828
905
1017
1050
1052
1057
1081
error bar (1 σ)
Mg# & Cr#
0.86 OL Mg# 0.91
0.16 SPL Cr# 0.26
.204
.908
.179
.902
.234
.895
.234
.905
.179
.896
.195
.896
.213
.900
.168
.870
δlog(fO2)FMQ
-1
0
+1
-0.49
+0.19
+0.08
-1.27
+0.31
+0.39
+0.32
+0.69
Grain size of olivine
0.2
(mm)
0.6
0.47
0.47
0.38
0.29
0.30
0.21
0.26
0.53
Texture
Granular
Porphyroclastic
Al phases
PL (SYMP) + SPL
SPL
Hydrous mineral
AMP
Melt / fluid
Fluid
Melt
Subsolidus
Supersolidus
Interpretation
Crust
MOHO
ca. 25 km
Lithospheric mantle
ca. 40 km
Upper limit of LABZ
Lithosphere-Asthenosphere Boundary Zone
Lower limit of LABZ?
ca. 60 km
Asthenosphere

Figure 9.

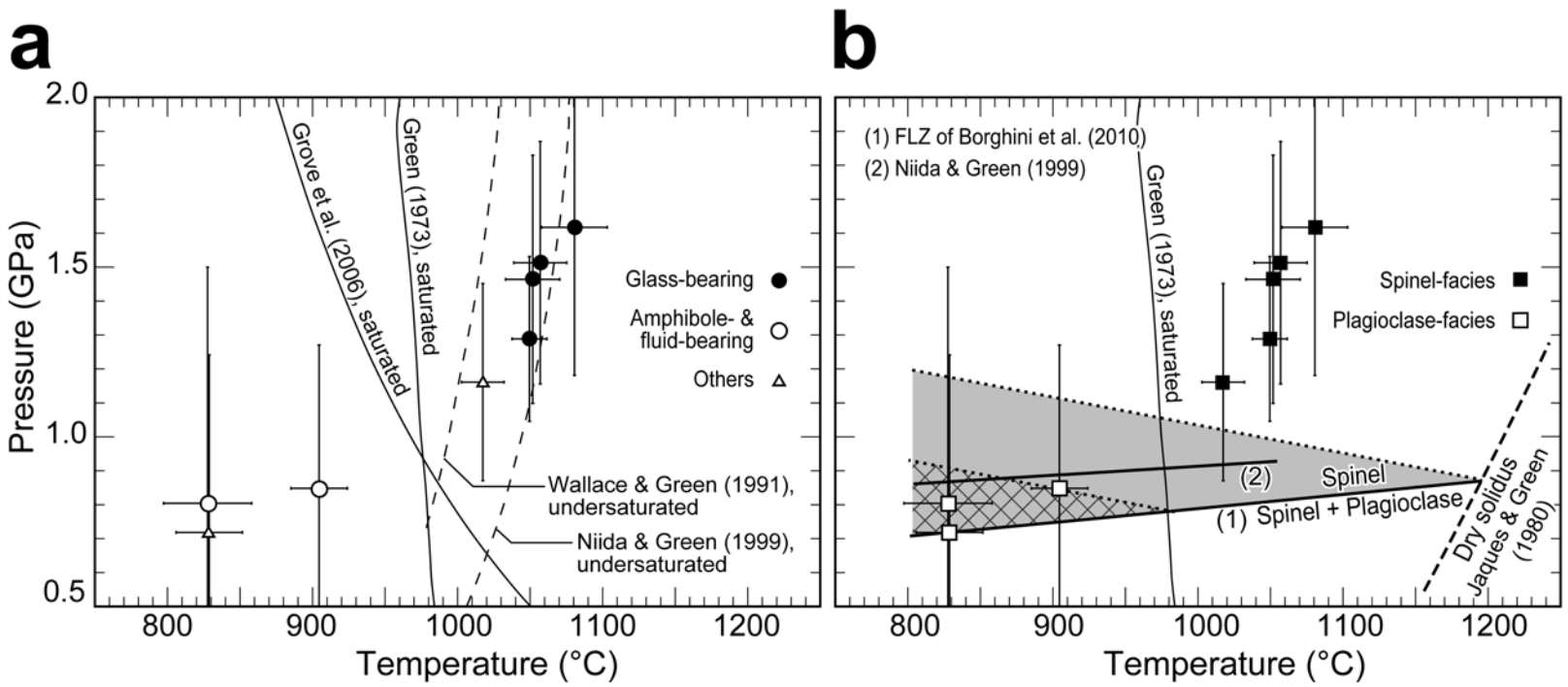
a
b
Pressure (GPa)
Temperature (°C)
Grove et al. (2006), saturated
Green (1973), saturated
Glass-bearing
Amphibole- & fluid-bearing
Others
Wallace & Green (1991), undersaturated
Niida & Green (1999), undersaturated
(1) FLZ of Borghini et al. (2010)
(2) Niida & Green (1999)
Spinel-facies
Plagioclase-facies
(2) Spinel
(1) Spinel + Plagioclase
Dry solidus Jaques & Green (1980)

Figure 10.

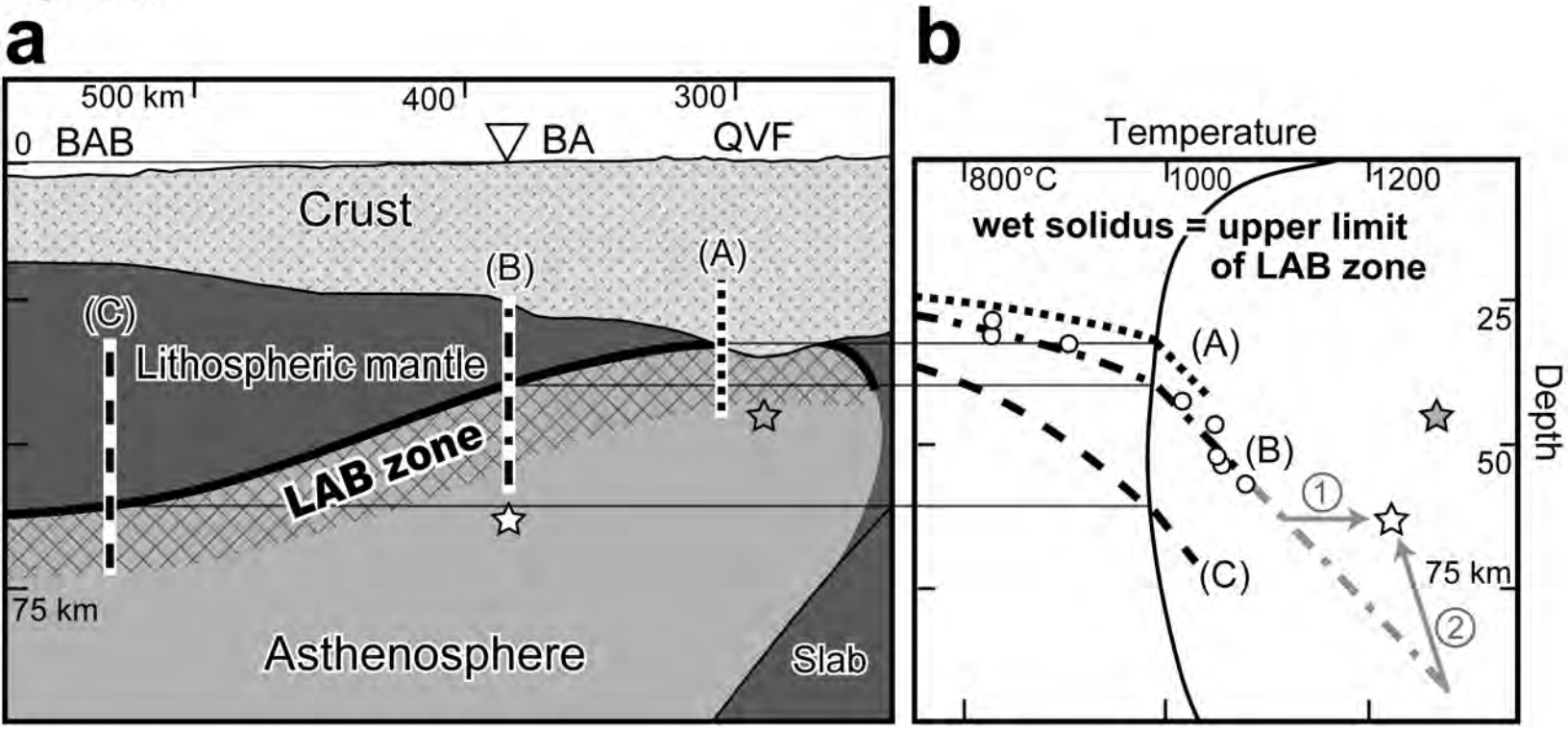
a
500 km
400
300
0 BAB
BA
QVF
Crust
(B)
(A)
(C)
Lithospheric mantle
LAB zone
75 km
Asthenosphere
Slab
b
Temperature
800°C
1000
1200
wet solidus = upper limit
of LAB zone
(A)
(B)
(C)
25
50
Depth
①
②
75 km